11-2021

STRENGTHENING OF CONCRETE DEEP BEAMS USING CARBON FABRIC REINFORCED CEMENTITIOUS/GEOPOLYMERIC MATRIX

Nour Mohamed Muhsen Khir Allah

United Arab Emirates University

College of Engineering

Department of Civil and Environmental Engineering

STRENGTHENING OF CONCRETE DEEP BEAMS USING CARBON FABRIC REINFORCED CEMENTITIOUS/GEOPOLYMERIC MATRIX

Nour Mohamed Muhsen Khir Allah

This thesis is submitted in partial fulfilment of the requirements for the degree of Master of Science in Civil Engineering

Under the Supervision of Professor Tamer El Maaddawy

November 2021

Declaration of Original Work

I, Nour Mohamed Muhsen Khir Allah, the undersigned, a graduate student at the United Arab Emirates University (UAEU), and the author of this thesis entitled *"Strengthening of Concrete Deep Beams Using Carbon Fabric Reinforced Cementitious/Geopolymeric Matrix"*, hereby, solemnly declare that this thesis is my own original research work that has been done and prepared by me under the supervision of Professor Tamer El Maaddawy, in the College of Engineering at UAEU. This work has not previously been presented or published, or formed the basis for the award of any academic degree, diploma or a similar title at this or any other university. Any materials borrowed from other sources (whether published or unpublished) and relied upon or included in my thesis have been properly cited and acknowledged in accordance with appropriate academic conventions. I further declare that there is no potential conflict of interest with respect to the research, data collection, authorship, presentation and/or publication of this thesis.

Student's Signature: _____ Date: ___11/11/2021_____

Advisory Committee

1) Advisor: Tamer El Maaddawy

Title: Professor

Department of Civil and Environmental Engineering

College of Engineering

2) Co-advisor: Hilal El Hassan

Title: Associate Professor

Department of Civil and Environmental Engineering

College of Engineering

Approval of the Master Thesis

This Master Thesis is approved by the following Examining Committee Members:

1) Advisor (Committee Chair): Tamer El Maaddawy

   Title: Professor

   Department of Civil and Environmental Engineering

   College of Engineering

   Signature _____ Date Dec. 5, 2021

2) Member: Bilal El-Ariss

   Title: Associate Professor

   Department of Civil and Environmental Engineering

   College of Engineering

   Signature _____ Date December 06, 2021

3) Member (External Examiner): Muhammad Hadi

   Title: Associate Professor

   School of Civil, Mining and Environmental Engineering

   Faculty of Engineering and Information Sciences

   University of Wollongong, Australia

on behalf of External Examiner

   Signature _____ Date December 06, 2021

This Master Thesis is accepted by:

Dean of the College of Engineering: Professor James Klausner

Signature James F. Klausner Date 7/12/2021

Dean of the College of Graduate Studies: Professor Ali Hassan Al-Marzouqi

Signature Ali Hassan Date 7/12/2021

Copy ____ of ____

Abstract

This research aimed to examine the effectiveness of using carbon fabric-reinforced matrix (C-FRM) composites to improve the shear response of reinforced concrete (RC) deep beams. Ten RC deep beams with *a/h* of 1.6 were tested, where *a* is the shear span and *h* is the beam depth. Test parameters included the presence of internal shear reinforcement (no shear reinforcement and minimum shear reinforcement), number of C-FRM composite layers (one and two layers), angle of inclination of the second layer of CFRM (90^o and 0^o with respect to the longitudinal direction of the beam), and type of matrix (cementitious and geopolymeric). In the absence of internal shear reinforcement, the use of one layer of C-FRM with cementitious and geopolymeric matrices resulted in 95% and 77% increases in the shear capacity, respectively. The shear capacity of the specimens strengthened with two layers of C-FRM composites were insignificantly higher than that of their counterparts strengthened with one layer of C-FRM. Positioning the second layer of CFRM in the vertical direction (i.e., at angle of inclination of 90^o) tended to be more effective than placing it in the horizontal direction (i.e., at angle of inclination of 0^o). The gain in shear capacity was less pronounced in the presence of internal shear reinforcement where a maximum shear strength gain of 18% was recorded. Three-dimensional numerical models were developed to predict the shear response of the tested specimens. The shear capacities predicted numerically were in good agreement with those obtained from the tests. The ratio of the predicted-to-measured shear capacity was on average 0.90 with a corresponding standard deviation of 0.09 and a coefficient of variation of 10%.

Keywords: deep beams, shear, strengthening, carbon, fabrics, composites, cementitious, geopolymeric.

Title and Abstract (in Arabic)

تقوية الجسور الخرسانية العميقة باستخدام المونة الاسمنتية/الجيوبوليمرية المسلحة بنسيج الألياف الكربونية

الملخص

يهدف هذا البحث إلى فحص فعالية استخدام مركبات مصفوفة الكربون المقوى (CFRM) لتحسين استجابة القص للحزم العميقة للخرسانة المسلحة (RC). تم اختبار عشرة عوارض عميقة RC مع نسبة امتداد القص إلى العمق 1.6 (a / h). تضمنت معلمات الاختبار وجود تقوية القص الداخلية (لا يوجد تقوية للقص وأقل تقوية للقص) ، وعدد الطبقات المركبة CFRM (طبقة واحدة وطبقتين) ، وزاوية ميل الطبقة الثانية من CFRM (90 درجة و 0 درجة فيما يتعلق بالاتجاه الطولي) من الشعاع) ، ونوع المصفوفة (اسمنتية وجيوبوليمرية). في غياب تعزيز القص الداخلي، أدى استخدام طبقة واحدة من CFRM مع المصفوفات الأسمنتية والجيوبوليمرية إلى زيادة 95 و 77 ٪ في قدرة القص ، على التوالي. كانت قدرة القص للعينات المعززة بطبقتين من مركبات CFRM أعلى بشكل ضئيل من نظيراتها المقواة بطبقة واحدة من CFRM. يميل وضع الطبقة الثانية من CFRM في الاتجاه العمودي (أي بزاوية ميل 90 درجة) إلى أن يكون أكثر فعالية من وضعه في الاتجاه الأفقي (أي بزاوية ميل 0 درجة). كان الكسب في قدرة القص أقل وضوحًا في وجود تقوية القص الداخلية حيث تم تسجيل أقصى كسب لمقاومة القص بنسبة 18٪. تم تطوير نماذج محاكاة عددية ثلاثية الأبعاد للتنبؤ باستجابة القص للعينات المختبرة. كانت قدرات القص المتوقعة عدديًا متوافقة جيدًا مع تلك التي تم الحصول عليها من الاختبارات. كانت نسبة سعة القص المتوقعة إلى المقاسة في المتوسط 0.90 مع الانحراف المعياري المقابل 0.09 ومعامل التباين 10٪.

مفاهيم البحث الرئيسية: عوارض عميقة، قص ، تقوية ، كربون ، أقمشة ، مركبات ، أسمنتية ، جيوبوليمير.

Acknowledgements

First of all, I would like to thank Allah for letting me through all the difficulties.

I would like to acknowledge and give my warmest thanks to my supervisor Prof. Tamer El Maaddawy, who made this work possible. His guidance and advice carried me through all the stages of my research. I would also like to thank Dr. Hilal for his support and guidance.

I would also like to give special thanks to my family for their continuous support and understanding when undertaking my research and writing my thesis.

Finally, I would like to thank all my colleagues who have encouraged and helped me finished this research through these years.

Dedication

To my beloved parents, sister, brothers, sister-in-law, nephew, and niece

Table of Contents

Title i
Declaration of Original Work ii
Advisory Committee iv
Approval of the Master Thesis v
Abstract vii
Title and Abstract (in Arabic) viii
Acknowledgements ix
Dedication x
Table of Contents xi
List of Tables xiv
List of Figures xv
List of Abbreviations xviii
Chapter 1 : Introduction 1
1.1 Background 1
1.2 Scope and Objectives 2
1.3 Thesis Organization 2
Chapter 2 : Literature Review 4
2.1 Introduction 4
2.2 FRCM Strengthening System 4
2.2.1 Introduction 4
2.2.2 Factors Affecting the Performance in Shear Strengthen 5
2.3 Shear Strengthening with FRCM 8
2.3.1 Slender Beams 8
2.3.2 Deep Beams 11
2.4 Geopolymer Matrix as a Sustainable Alternative to Commercial Mortars 14
2.5 Research Significance 14
2.6 Summary 15
Chapter 3 : Experimental Program 16
3.1 Introduction 16
3.2 Test Program 16
3.3 Details of Test Specimens 18
3.4 Material Properties 20
3.4.1 Concrete 20
3.4.2 Steel Reinforcement 21

3.4.3 FRCM 22
3.4.4 Cementitious Mortar 23
3.4.5 Geopolymer Mortar 23
3.5 Specimens Fabrication 24
3.5.1 Reinforcing Cages and Formwork 24
3.5.2 Steel Strain Gauges 25
3.5.3 Concrete Casting 26
3.5.4 FRCM/FRGM Strengthening 28
3.6 Instrumentation and Testing 31
3.7 Summary 33

Chapter 4 : Experimental Results 34
4.1 Introduction 34
4.2 Shear Load-Deflection Response 34
4.2.1 Control Un-strengthened Specimens 34
4.2.2 Strengthened Specimens of Group A 35
4.2.3 Strengthened Specimens of Group B 37
4.2.4 Strengthened Specimens of Group C 38
4.3 Crack Pattern and Failure Mode 40
4.3.1 Un-strengthened Specimens 40
4.3.2 Strengthened Specimens of Group A 42
4.3.3 Strengthened Specimens of Group B 45
4.3.4 Strengthened Specimens of Group C 48
4.4 Performance Evaluation 50
4.5 Strain Measurements 52
4.5.1 Steel Strains 52
4.5.2 Stirrup Steel Strains 57
4.5.3 Carbon Fabric Strains 59
4.5.4 Concrete Strains 62
4.6 Summary 64

Chapter 5 : Numerical Modeling and Simulation 65
5.1 Introduction 65
5.2 Material Constitutive Laws 65
5.2.1 Concrete Constitutive Models 65
5.2.2 Steel Stress-Strain Response 70
5.2.3 Carbon fabric Stress-Strain Response 71
5.2.4 Bod-Slip Model 72
5.3 Element Types 73
5.4 Monitoring Points 74
5.5 Boundary Conditions and Loading 76
5.6 Comparative Analysis 76
5.6.1 Shear Load-Deflection Response 79
5.6.2 Crack Pattern 85

5.6.3 Strains at Peak Load 86
5.7 Summary 93

Chapter 6 : Conclusions and Recommendations 94
6.1 Introduction 94
6.2 Limitations of the Current Study 95
6.3 Conclusions 95
6.4 Recommendations for Future Studies 97

References 98

List of Tables

Table 3.1: Test matrix 17
Table 3.2: Mix proportions for concrete 20
Table 3.3: Results of concrete strength tests 21
Table 3.4: Properties of steel bars 22
Table 3.5: Carbon-fiber mesh properties 23
Table 3.6: Geopolymeric matrix components and proportions 24
Table 4.1: Test results of the control un-strengthened specimens 35
Table 4.2: Test results of specimens of group A 37
Table 4.3: Test results of specimens of group B 38
Table 4.4: Test results of specimens of group C 39
Table 4.5: Summary of test results 52
Table 4.6: Maximum measured strain in steel reinforcement 56
Table 4.7: Maximum concrete strains at shear capacity 63
Table 5.1: Concrete properties 70
Table 5.2: Properties of cementitious mortar 70
Table 5.3: Properties of geopolymeric mortar 70
Table 5.4: Input parameters of monitoring points 75
Table 5.5: Comparison between numerical and experimental results 79
Table 5.6: Strains at peak load for models with perfect bond 88
Table 5.7: Strains at peak load for models with bond-slip law 88

List of Figures

Figure 3.1: Details of a typical specimen without internal shear reinforcement (dimensions in mm) 19
Figure 3.2: Details of a typical specimen with internal shear reinforcement (dimensions in mm) 19
Figure 3.3: Concrete samples during testing: A. Cylinders comrpesion test, B. Splitting test, C. Cube comrpesion test 21
Figure 3.4: Fibers mesh 22
Figure 3.5: Steel cages of the beams with stirrups 24
Figure 3.6: Steel cages of the beams without stirrups 24
Figure 3.7: Formwork of the beams 25
Figure 3.8: Locations of longitudinal steel strain gauges 25
Figure 3.9: Locations of steel strain gauges on internal shear reinforcement 26
Figure 3.10: Installation of strain gauges: A. Materials used, B. Bonding strain gauges to steel bars 26
Figure 3.11: Steel cages inside the forms 27
Figure 3.12: Concrete casting: A. Ready-mix concrete truck, B. Placement of concrete, C. Vibration of concrete 27
Figure 3.13: Finsising and curing: A. Leveling the concrete surface, B. Beams covered with burlaps, C. Spraying water for curing 27
Figure 3.14: Prepartion of fabrics: A. Cutting the fabric mesh, B. Prepared carbon fabric 28
Figure 3.15: Installing the stain gauges on the fiber: A. An adhesive on the fabric for surface preparation, B. Fabric with a strain gauge installed 28
Figure 3.16: Concrete surface prepartion: A. Use of water jet for surface preparation, B. Concrete after surface roughening 29
Figure 3.17: Preparation of the cementitious mortar: A. Solid cementitious material, B. Mixing of mortar 29
Figure 3.18: Application of FRCM composites: A. Application of first layer of mortar, B. Placement and impregnation of the fabric, C. Application of the second layer of mortar, D. Leveling of the concrete surface 30
Figure 3.19: Curing of of FRCM composites: A. Beams covered with burlaps, B. Spraying water on the burlaps 30
Figure 3.20: Preparation of the geopolymeric matrix: A. Solid materials, B. Alkaline activator solution, C. Geopolymeric mixture 31
Figure 3.21: Application of FRGM composites: A. First layer of geopolymer, B. Impregnation of fabric, C. Second layer of geopolymer, D. Finished surface 31
Figure 3.22: Positions of concrete strain gauges positions 32

Figure 3.23: Test setup 32
Figure 3.24: A test in progress 33
Figure 4.1: Shear load-deflection response of the control specimens 35
Figure 4.2: Shear load-deflection response of specimens of group A 36
Figure 4.3: Shear load-deflection response for specimens of group B 38
Figure 4.4: Shear load-deflection response for specimens of group C 39
Figure 4.5: Crack pattern of specimen Control-NS: A. Schematic drawing of the crack pattern, B. Picture of the beam at failure, C. Close view of the crack pattern (west shear span) 41
Figure 4.6: Crack pattern of specimen Control-ST: A. Schematic drawing of the crack pattern, B. Picture of the beam at failure, C. Close view of the crack pattern (west shear span) 42
Figure 4.7: Crack pattern of specimen NS-C1-90: A. Schematic drawing of the crack pattern, B. Picture of the beam at failure, C. Close view of the crack pattern (west shear span) 43
Figure 4.8: Crack pattern of specimen NS-C2-90: A. Schematic drawing of the crack pattern, B. Picture of the beam at failure, C. Close view of the crack pattern (west shear span) 44
Figure 4.9: Crack pattern of specimen NS-C2-0/90: A. Schematic drawing of the crack pattern, B. Picture of the beam at failure, C. Close view of the crack pattern (east shear span) 45
Figure 4.10: Crack pattern of specimen ST-C1-90: A. Schematic drawing of the crack pattern, B. Picture of the beam at failure, C. Close view of the crack pattern (east shear span) 46
Figure 4.11: Crack pattern of specimen ST-C2-90: A. Schematic drawing of the crack pattern, B. Picture of the beam at failure, C. Close view of the crack pattern (east shear span) 47
Figure 4.12: Crack pattern of specimen ST-C2-0/90: A. Schematic drawing of the crack pattern, B. Picture of the beam at failure, C. Close view of the crack pattern (east shear span) 48
Figure 4.13: Crack pattern of specimen NS-G1-90: A. Picture of the beam at failure, B. Close views at failure (east shear span) 49
Figure 4.14: Crack pattern of specimen ST-G1-90: A. Picture of the beam at failure, B. Close views of the crack pattern (west shear span) 49
Figure 4.15: Steel strain profile of un-strengthened specimens: A. Specimen Control - NS, B. Specimen Control – ST 53
Figure 4.16: Steel strain profile of specimens of group A: A. Specimen NS-C2-90, B. Specimen NS-C2-0/90 54
Figure 4.17: Steel strain profile of specimens of group B: A. Specimen ST-C1-90, B. Specimen ST-C2-90, C. Specimen ST-C2-0/90 55
Figure 4.18: Steel strain profile of specimens of group C: A. Specimen NS-G1-90, B. Specimen ST-G1-90 56

Figure 4.19: Stirrup strain response of specimen Control-ST 57
Figure 4.20: Stirrup strain response of specimen ST-C1-90..... 58
Figure 4.21: Stirrup strain response of specimen ST-C2-0/90..... 58
Figure 4.22: Stirrup strain response of specimen ST-G1-90 58
Figure 4.23: Carbon fabric strain response of specimens of group A: A. Specimen NS-C1-90, B. Specimen NS-C2-90, C. Specimen NS-C2-0/90..... 60
Figure 4.24: Carbon fabric strain response of specimens of group B: A. Specimen ST-C1-90, B. Specimen ST-C2-90, C. Specimen ST-C2-0/90 61
Figure 4.25: Carbon fabric strain response of specimens of group C: A. Specimen NS-G1-90, B. Specimen ST-G1-90 62
Figure 5.1: Concrete tensile softening 67
Figure 5.2: Concrete compressive hardening behavior..... 68
Figure 5.3: Concrete compressive softening..... 69
Figure 5.4: Stress-strain of the steel with strain hardening..... 71
Figure 5.5: Stress-strain response of carbon fabric..... 72
Figure 5.6: Bond-slip models at the fabric-matrix interface..... 73
Figure 5.7: Finite element model layout of beams without stirrups 74
Figure 5.8: Finite element model layout of beams with stirrups 74
Figure 5.9: Finite element model layout of strengthened beams 74
Figure 5.10: Locations of monitoring points: A. Models without stirrups, B. Models with stirrups 75
Figure 5.11: Supports and prescribed displacement 76
Figure 5.12: Shear load-deflection response of the control specimens..... 81
Figure 5.13: Shear load-deflection response for specimens of group A 82
Figure 5.14: Shear load-deflection response for specimens of group B 83
Figure 5.15: Shear load-deflection response for specimens of group C 84
Figure 5.16: Crack pattern of un-strengthened specimens..... 85
Figure 5.17: Crack pattern of specimens of group A..... 86
Figure 5.18: Crack pattern of specimens of group B 86
Figure 5.19: Crack pattern of specimens of group C 86
Figure 5.20: Steel stirrup strain response of the models with perfect bond..... 89
Figure 5.21: Steel stirrup strain response of the models with bond-slip law..... 90
Figure 5.22: Carbon fabric strain response of the models with perfect bond 91
Figure 5.23: Carbon fabric strain response of the models with bond-slip law 92

List of Abbreviations

ACI	American Concrete Institute
A_v	Area of the stirrups
A_{vh}	Area of horizontal stirrups reinforcement
a/h	Shear span to depth ratio
a/d	Shear span to effective depth ratio
a_g	The maximum aggregate size
b_w	The width of the web of the beam
CFRCM	Carbon fabric
d	Effective depth
d’	The distance longitudinal compression steel
E_s	Young’s modulus of steel
E_c	The concrete modulus of elasticity
E	East
FRCM	Fabric-reinforced cementitious matrix
FE	Finite element
f_y	Steel yield strength
f_t	The concrete tensile strength
f'_t	The uniaxial concrete tensile strength
f'_c	Concrete cylinder compressive strength
f'_{co}	Compressive stress
G_f	Unit area of stress-free crack
LVDTs	Linear variable differential transducers
L_t	The crack band length

NS	No stirrups
OPC	Ordinary Portland Cement
r_c	Compressive strength reduction factor
ST	With stirrups
SS	Sodium silicate
SH	Sodium hydroxide
s	Spacing of the stirrups
s_2	Spacing of horizontal reinforcement
V_{Exp}	Experimental load capacity
V_{FE}	Predicted load capacity by numerical model
W	West
w/c	Water-cement ratios
w_t	The crack opening displacement
w_{tc}	Crack opening at complete release stress
w	The maximum crack width
w_d	The plastic displacement
3D	Three-dimensional
ρ_v	The shear reinforcement ratio in the vertical direction
ρ_h	The shear reinforcement ratio in the horizontal direction
με	Micro strain
$\varepsilon_{s,max}$	Maximum strain
ε_y	Yield strain
ε_f	The fracturing strain
ε_p	Plastic strain

ε_{cp}	Plastic strain at compressive strength
σ_t	Tensile stress
σ_c	Compressive stress
τ_{ef}	The shear strength of a cracked concrete

Chapter 1 : Introduction

1.1 Background

Deep beams are widely used in structural building as a pile cap, transfer girder, panel beam, or strap beam in the foundation. Deep beams may be defined as those with concentrated loads within two times the distance of the member's depth from the support's face (i.e., $a/h \leq 2$) [1]. Slender beams transfer the vertical load to the support by combining bending and shear actions of the beam, whereas deep beams transfer the loads directly to the support through the arch action effect.

Fabric-reinforced cementitious matrix (FRCM) composites are a new technology used to repair and enhance the performance of concrete and masonry constructions. The cementitious matrix of FRCM exhibits the following qualities, which are the main reasons for considering it as a helpful strengthening material: a) Heat resistance built-in b) Substrate compatibility c) Long-term durability [2].

There is a potential to use a geopolymeric matrix in FRCM composites as a sustainable alternative to commercial mortars. Cement manufacturing generates a significant amount of carbon dioxide. It also consumes non-renewable natural resources. Therefore, a small number of researchers looked into the possibility of using cement-free geopolymeric matrices instead of cementitious mortars to create sustainable fabric-reinforced geopolymeric matrix (FRGM) strengthening solutions to resolve these concerns [3].

1.2 Scope and Objectives

The aim of this research is to investigate the non-linear behavior of concrete deep beams strengthened with carbon fabric-reinforced matrix. The study embarks on the following objectives:

1. Examine the effectiveness of using fabric-reinforced geopolymeric matrix system as a sustainable solution to improve the structural response of deep beams in concrete structures.

2. Study the effect of the presence of stirrups and varying the amount and orientation of the fabric layers on the behavior of deep beams strengthened with carbon fabric-reinforced cementitious matrix system.

3. Develop 3D finite element models capable of simulating the nonlinear behavior of deep beams strengthened with fabric-reinforced cementitious/geopolymeric matrix system.

4. Examine the accuracy and validity of the numerical simulation models to predict the behavior of deep beams strengthened with carbon fabric-reinforced matrix system.

1.3 Thesis Organization

Chapter 1 introduces a general background about the research topic, including the characteristics and applications of deep beams, strengthening method for deep beams with FRCM system, and the research scope and objectives.

In Chapter 2, an overview of the reviewed literature related to this study is presented. The chapter presents the FRCM strengthening system, shear strengthening

with FRCM, geopolymer matrix as a sustainable alternative to commercial mortars, and research significance.

The experimental program is covered in Chapter 3, including the test program, details of test specimens, specimen fabrication, and instrumentation and testing setup. In addition, materials properties and strengthening techniques are also provided in this chapter.

Chapter 4 shows the experimental results of testing deep beam specimens. Also, shear load-deflection response, crack pattern, failure mode, data analysis, and strain measurements are shown in this chapter.

Details of the developed numerical models of the test specimens using ATENA 3D is presented in Chapter 5. At the end of the chapter, a comparison of numerical and experimental results is shown.

Chapter 6 provides a summary of the present research work, general conclusions, and recommendations for future studies.

Chapter 2 : Literature Review

2.1 Introduction

Shear strengthening of concrete structures is frequently required to accommodate additional loads not taken in the initial design. This chapter introduces a summary of outcomes of previous research related to shear strengthening of concrete beams using FRCM system. The importance of using cement-free geopolymer matrix instead of commercial mortars is highlighted. Research significance is provided at the end of the chapter.

2.2 FRCM Strengthening System

2.2.1 Introduction

American Concrete Institute (ACI) [2] presents FRCM composites as a new technology used to repair and enhance concrete and masonry constructions. Existing concrete and masonry structures have traditionally been restored and rehabilitated utilizing new and old materials and construction techniques, such as externally bonded fiber-reinforced polymer (FRP) systems, steel plates, reinforced concrete (RC) overlays, and post-tensioning. The cementitious matrix of FRCM exhibits the following qualities, which are the main reasons for considering it as a helpful strengthening material: a) Heat resistance built-in b) Substrate compatibility c) Long-term durability. The following sections present a review of the available literature on shear strengthening with FRCM.

2.2.2 Factors Affecting the Performance in Shear Strengthen

2.2.2.1 Method Description

Koutas et al. [4] indicated that shear strengthening of RC beams or bridge girders is frequently required due to the absence of shear reinforcement, existing shear reinforcement corrosion, low concrete strength, and/or an increase in the applied load. Furthermore, in order to provide a ductile flexure-type failure mode, shear strengthening is also significant. Therefore, FRCM is applied as side-bonding, U-wrapping, or full wrapping at critical shear spans. In addition, mechanical devices, spike or textile-based anchors, and other anchorage techniques have also been employed to improve the anchorage conditions of side-bonded and U-shaped jackets.

2.2.2.2 Failure Modes

Four FRCM modes of failure were reported by Awani et al. [5]. The first failure mode was cover separation due to the creation of longitudinal cracks on the beams' top and/or bottom surfaces, preceded by the formation of several shear cracks in the shear span. The longitudinal cracks developed as the load increased, eventually resulting in the separation of the lateral concrete coverings of the beam. A difference in stiffness between the FRCM reinforcement and the concrete substrate may have caused a stress concentration and significant interfacial stresses between the lateral cover and the concrete core, resulting in this failure mode. The second reported failure mode was debonding at the concrete-matrix interface: a smooth separation of the strengthening layer from the concrete or a layer of concrete attached could cause debonding failure at the concrete-matrix contact. This failure mode was observed in specimens with a high FRCM reinforcement ratio (four to six layers). In addition, the high flexural

rigidity of the FRCM jacket caused unsuitable deformations with the concrete substrate, resulting in premature debonding at the concrete-matrix interface. the third failure mode was slippage of fabric roving within the matrix due to a lack of interlock between the mortar and the fabric was attributed to this failure mode. The interlock was enhanced when two to three layers were applied, and failure was moved to the separation of the concrete cover. The fourth failure mode was rupture of the fabric within the matrix at locations where shear cracks crossed the fabric roving. The fabric strains approached the fibers' ultimate strain, indicating a good connection between the fabric and the mortar. The presence of mechanical anchorage could also cause fabric rupture near the anchors.

2.2.2.3 Factors Affecting the Shear Capacity of FRCM Strengthened Beams

The improvement of the shear capacity of FRCM-strengthened RC beams is affected by the following factors [5]:

1) Number of FRCM layers (reinforcement ratio): Increasing the number of layers leads to a non-proportional rise in shear capacity. As a result, a denser mesh pattern is formed with two or more layers, resulting in improved mechanical interlock in the FRCM system and preventing premature fabric failure.

2) Fabric type: The structural response of FRCM shear strengthened elements is influenced by fabric geometry and fiber type. A higher number of fibers in the fabric rovings resulted in a more significant increase in strength.

3) Mortar type: The use of polymer-modified mortars or the introduction of fibers in mortars increased the performance of FRCM strengthening systems in enhancing the shear resistance of RC beams. Specimens constructed with polymer-

modified mortar gained up to 69% more strength than those made with ordinary cementitious mortar.

4) FRCM configuration: The rovings are typically placed perpendicular to the beam axis in the standard configuration of FRCM systems in shear strengthening of RC beams. However, the rovings can also be set at an angle to the beam axis in a spiral application. There was no significant difference in performance between the spiral and conventional layouts. In FRCM shear strengthening, U-shaped fabric wrapping could provide a more remarkable shear strength improvement than lateral fabric application. Full wrapping of the FRCM composite successfully changes the failure mode from shear to flexural. On the other hand, this configuration is less cost-effective and may not be practicable in some situations.

5) Mechanical anchorage: Fabric rovings pulled out of the anchored specimens, which caused them to fail. However, when mechanical anchors were present, the FRCM system's effectiveness in improving shear capacity increased, with even more improvement when the anchor spacing was reduced. Thus, the change in the failure mode can be assigned to the enhanced performance of the specimens with mechanical anchorage. In addition, the presence of mechanical anchorage stopped the beams from fast debonding, allowing them to develop greater shear capacity.

6) Stirrup spacing: Shear-strength enhancement was lower in specimens with more internal steel stirrups because these specimens had higher original shear resistance.

2.3 Shear Strengthening with FRCM

Numerous investigations studied the shear behavior of slender RC beams strengthened with a fabric-reinforced cementitious matrix (FRCM) strengthening system. Shear strengthening with the FRCM system reduced the deflection at service loads, delayed yielding of stirrups, and reduced surface cracks, thus offering a substantial increase in the shear resistance. Few studies focused on the shear behavior of RC deep beams strengthened with the FRCM strengthening system.

2.3.1 Slender Beams

This section review of the available literature on shear strengthening of slender RC beams with FRCM.

Awani et al. [6] investigated the shear behavior of RC beams with *a/d* of 3 (i.e. *a/h* = 2.5) strengthened in shear using Carbon-FRCM composites. The study comprised experimental testing and numerical modeling. Test variables included the type of matrix (cementitious and epoxy), number of FRCM layers (one and two layers), and the spacing between internal stirrups (0.3 *d* and 0.6 *d*, where *d* = effective depth of the tension steel). Test results showed that shear strengthening limited the crack width, reduced the rate of increase of stirrup strains, and delayed yielding of stirrups. The use of epoxy as a matrix rather than a cementitious mortar in significantly increased the shear strength gain. The strain of FRCM at peak load appeared to decrease with an increase in the number of FRCM layers. The shear strength gain due to FRCM strengthening for the beams with stirrups was in the range of 51% to 67% whereas beams without stirrups exhibited up to a 130% increase in the shear capacity. Increasing the number of FRCM layers had an almost no effect on the shear strength

gain of the beams with stirrups but resulted in a non-proportional increase in the shear strength gain for the beams without stirrups. increase the has resulted in a non-proportional improvement in the shear strength gain. The researchers adopted two approaches in the numerical modeling; the detailed approach, which involved modeling both the fabric and the matrix, and a simplified approach in which the fabric was modeled as discrete reinforcement bonded directly to the beam surface without a binder. No significant difference in numerical results was reported. The shear response of the beams predicted numerically was in good agreement with that obtained from the experimental tests.

Aljazaeri and Myers [7] investigated the behavior of RC beams with *a/d* of 2.7 (i.e., *a/h* = 2.2) strengthened in shear using PBO-FRCM composites. Test parameters included the strengthening scheme (continuous and strips), number of FRCM layer, and the presence of stirrups. The increase in the shear capacity due to strengthening for the beams with stirrups was in the range of 18% to 32% relative to the that of the control beam. The continuous FRCM scheme was more effective in improving the shear resistance than the strips scheme. For the beams without stirrups, no or insignificant increase the shear capacity was reported. This was attributed to the reduced contribution of the aggregate interlock in the absence of stirrups which resulted in rapid failure of the FRCM and a reduced shear strength gain. The authors reported that additional tests are needed to increase the current experimental database.

Gonzalez-Libreros et al. [8] conducted an investigation to examine the shear behavior of RC beams, with *a/d* of 3 (i.e., *a/h* = 2.5), strengthened with externally-bonded composites. Two different composite types were used in strengthening, namely, FRP and FRCM. The reinforcement used in FRCM consisted of either carbon

fabrics or steel fibers. Two different internal shear reinforcement ratios were adopted. Test results demonstrated that a higher gain in the shear capacity was recorded with an increase in the axial stiffness of the composite. The improvement in shear strength was comparable for the steel FRP and FRCM reinforced beams. The efficacy of the FRCM composite was affected by the internal shear reinforcement ratio (i.e., stirrups spacing). Beams with a greater stirrup spacing (i.e., lower internal shear reinforcement ratio) exhibited a more significant increase in shear capacity than that exhibited by a similar beam with less stirrups spacing (i.e., greater internal shear reinforcement ratio). Beams strengthened with carbon FRCM failed by a local separation of the entire composite layer or due to slippage of the fiber along the main crack. Debonding at the matrix-concrete interface (i.e., separation of the composite layer) was the dominate failure mode for the beams strengthened with steel FRCM. All beams exhibited shear cracks on the surface of the FRCM composite prior to failure. The internal-external shear reinforcement interaction was less noticeable for the beams with FRCM relative to that of the beams with FRP. The use of anchors did not significantly increase the shear strength gain although it mitigated a premature debonding of the composites in some beams. The highest fiber strain was significantly lower than the effective strain proposed by current available analytical models.

Azam et al. [9] presented examined the behavior of RC beams, with *a/d* of 3.15 (i.e. *a/h* = 2.5), strengthened in shear with carbon bi-directional FRCM composites. Some beams had no internal stirrups whereas other beams included stirrups at a spacing of either 150 mm or 250 mm. Test results showed that shear strengthening of CFRCM successfully enhanced the shear capacity. Beams without stirrups exhibited the highest increase in the shear capacity (87%). The efficiency of FRCM shear strengthening decreased in the presence of internal stirrups. Beams with stirrup spacing

of 250 mm exhibited a shear strength gain of 32%. The strength gain decreased with an increase in the amount of internal stirrups. Only 25% shear strength gain was recorded at a stirrup spacing of 150 mm. The CFRCM strain recorded at failure was on average 5,083 με, indicating that the CFRCM strain limit of 4,000 με specified by in ACI 549.4R-13 could be considered adequate for design.

2.3.2 Deep Beams

Younis et al. [10] investigated the effectiveness of using various FRCM composites to improve the shear behavior of RC beams with *a/d* of 2 (i.e., *a/h* = 1.7). The beams had no internal steel stirrups. Three types of fabrics were used in the FRCM, namely, carbon, glass, and PBO. The shear strengthening within the shear span consisted of continuous or intermitted FRCM composite layers. It was reported that the axial stiffness could be used to compare performance of FRCM-strengthened beams. The gain in the shear capacity caused by FRCM shear strengthening applied continuously within the shear span was in the range of 45% to 100%. The use of intermitted FRCM composite layers was less effective in improving the shear capacity. The strength gain for the beams with carbon, PBO, and glass intermitted FRCM was in the range of 45 to 70%; 32% to 55%; and 17% to 32%, respectively. The deformation characteristics were generally enhanced due to the use of FRCM. The deflection capacity was up to 2.4 times that recorded for the reference specimen. Strengthened beams demonstrated a typical failure mode pattern, i.e., the debonding of the strengthening layer. Beams with C-FRCM systems experienced smaller crack widths than those of their counterparts strengthened with PBO or G-FRCM systems. Also, the inclusion of an anchorage system had no impact of the shear capacity. The authors used an analytical approach based on ACI 549-13 [2] to estimate the

contribution of the FRMC to the shear resistance. Theoretically predicted shear capacity values were in a fair agreement with those obtained from the experiments.

Wakjira and Ebead [11] investigated the performance of FRCM-shear strengthened RC beams with a shear span-to-effective depth ratio (*a/d*) of 2, which corresponded to *a/h* of 1.7. Test parameters included the presence of internal transverse shear reinforcement (ITSR) inside the critical shear span (CSS) and type of fabric (carbon, glass, and polyparaphenylene benzobisoxazole (PBO)). It was concluded that the presence of ITSR within the CSS decreased the efficacy of the FRCM system. The overall average shear strength gain decreased from 59.5% to 30.7% due to the presence of ITSR. Carbon FRCM composite was more effective in improving the shear capacity than glass and PBO FRCM composites. This was attributed to its higher axial rigidity. Continuous FRCM configuration was more effective than the discontinuous configuration in improving the shear capacity. When the FRCM systems failed, the deformations were higher. Beams without ITSR in the CSS exhibited higher improvement in the deformation capacity than those exhibited by the beams having with ITSR. Failure of strengthened beams was governed by fabric rupture with no signs of FRCM/concrete debonding or delamination within the FRCM. Debonding of FRCM was mitigated due to embedment of the FRCM layer with a surface layer in the concrete cover having a thickness of 15 mm thick. A model based on the simplistic compression field theory (SCFT) was used to estimate the reinforced beams' ultimate load-carrying capacity. The ratio between theoretical and experimental values of the load carrying capacity ranged from 83 to 124%.

Azam et al. [12] investigate the shear behavior of RC deep beams (*a/h* = 1.25 and *a/d* = 1.6) strengthened in shear with different FRCM systems. The strengthening

regimes included a CFRP grid in a cementitious mortar (CGM), carbon-FRCM (CM), and epoxy-based CFRP composite sheets (CP). A group of beams had internal stirrups at a spacing of 250 mm and another group had not internal shear reinforcement. The shear strength gain for the beams without stirrups was in the range of 13% to 23%. The beams with internal stirrups exhibited a shear strength gain in the range of 8 to 16%. All specimen failed by splitting of the diagonal strut. The researchers proposed a simplified approach to predict the capacity of the strengthened specimens using a stress limit of 0.64 f'_c for bottle-shaped struts intersected by transverse reinforcement. The proposed approach did not account for the number of composite layers, type or amount of composite reinforcement, or its properties. The researchers recommended to conduct further research to investigate the effect of these essential parameters on analytical predictions.

Wakjira and Ebead [13] investigate the effect of the position of FRCM strips relative to that of the internal stirrups on the shear strength gain of RC beams with *a/d* of 2 (i.e. *a/h* = 1.7) caused by different FRCM systems. The fabrics used in the FRCM were carbon, glass, or PBO. The FRCM layer were near-surface-embedded (NSE) or externally bonded (EB) on the concrete surface. The position of FRCM strips relative to that of the stirrups had insignificant effect on the shear strength gain of strengthened specimens. The EB-FRCM strengthened beams failed due to FRCM debonding from the concrete; however, there was no evidence of FRCM debonding in the NSE-FRCM strengthened beams. As a result, the gain in the shear capacity was on average 41% for the NSE-FRCM strengthened beams and 28% for the EB-FRCM strengthened beams. A simplified analytical approach was proposed to predict the shear capacity of the tested beams. There was a good agreement between analytical and experimental results.

2.4 Geopolymer Matrix as a Sustainable Alternative to Commercial Mortars

Manufacturing of cement generates a significant amount of carbon dioxide. It also consumes non-renewable natural resources. Therefore, a small number of researchers investigated the possibility of using cement-free geopolymeric matrices instead of cementitious mortars to create sustainable fabric-reinforced geopolymeric matrix (FRGM) strengthening solutions to resolve these concerns. Abu Obaida et al. [3] investigated the potential use of a geopolymeric matrix in carbon fabric-reinforced matrix composites as a sustainable alternative to commercial mortars. The geopolymeric matrix was made up of a mixture of fly ash and ground granulated blast furnace slag activated with an alkaline sodium silicate and sodium hydroxide solution. The bond behavior of specimens with a geopolymeric matrix was studied and compared to similar specimens with a cementitious matrix. Specimens with a geopolymeric matrix exhibited a bond behavior comparable to that of their counterparts with a cementitious mortar. The researchers developed bond-slip models that can characterize the bond behavior at the fabric-matrix interface for both types of matrices. Although both models had the same maximum shear stress (1.2 MPa), the slip at maximum shear stress of the geopolymeric-matrix model was higher (i.e., the cementitious matrix model exhibited a stiffer ascending branch).

2.5 Research Significance

Reinforced concrete deep beams (i.e., $a/h \leq 2$) are typically used as transfer girders in high-rise buildings. Loads in RC deep beams are transferred directly to the supports through concrete struts in the shear span (i.e., internal arch action effect). Shear strengthening of RC deep beams maybe required in practical setting due to insufficient maintenance, exposure to extreme loads, or deterioration caused by harsh

environments. To date, there is very little information available in the literature on the shear performance of large-scale RC deep beams with $a/h < 2$ strengthened with cementitious-based FRCM composites. There is also a need to investigate the potential use of cement-free geopolymer matrix to produce sustainable and eco-friendly carbon fabric-reinforced matrix systems for structural strengthening of RC deep beams before it can be routinely used in practical setting. This research aims to fill these gaps through experimental testing of large-scale RC deep beam specimens and numerical modeling. Development of innovative and sustainable solutions to solve complex structural engineering problems typically encountered in practical setting would support and advance sustainability of the economic activities and protect substantial investments in concrete infrastructure in UAE and worldwide.

2.6 Summary

This chapter provided an overview of previous studies on the shear strengthening of concrete beams with the FRCM system. It was emphasized the need to apply a cement-free geopolymer matrix instead of commercial mortars. The importance of the research was to fill the gaps by testing large-scale RC deep beam specimens, develop numerical simulation models for the tested beams, and perform comparative analysis. Details of the experimental program are given in the following chapter.

Chapter 3 : Experimental Program

3.1 Introduction

Large-scale RC deep beam specimens with *a/h* of 1.6 were constructed and tested to failure under a four-point bending configuration. Test variables included the presence of internal shear reinforcement (no shear reinforcement and minimum shear reinforcement), number of CFRM composite layers (one and two layers), angle of inclination of the second layer of CFRM (90^o and 0^o with respect to the longitudinal direction of the beam), and type of matrix (cementitious and geopolymeric). Details of the test matrix, material properties, deep beam specimens' fabrication, test setup, and instrumentation are presented in this chapter.

3.2 Test Program

The test matrix is presented in Table 3.1. The test program included a total of ten RC deep beam specimens with *a/h* of 1.6. The abbreviations "NS" in the designation of the specimen denotes no stirrups, while the "ST" refers to presence of stirrups. The symbols "C" and "G" refers to cementitious and geopolymeric matrix, respectively. The numbers "1" or "2" denote the number of strengthening layers, "90" refers to the angle inclination of the fabric in case of one or two layers in the vertical direction layers, and "0/90" refers to angle of inclination of the fabric in case of two layers; one in the vertical direction and one in the horizontal direction.

Table 3.1: Test matrix

Group	Type of matrix	Presence of internal stirrups	Number of FRCM layers	Angle of inclination of CFRCM	Designation
Control	-	-	-	-	Control-NS
	-	√	-	-	Control-ST
A	Cementitious	-	One layer	90-degree	NS-C1-90
			Two layers	90-degree	NS-C2-90
			Two layers	0/90-degree	NS-C2-0/90
B	Cementitious	√	One layer	90-degree	ST-C1-90
			Two layers	90-degree	ST-C2-90
			Two layers	0/90-degree	ST-C2-0/90
C	Geopolymer	-	One layer	90-degree	NS-G1-90
		√	One layer	90-degree	ST-G1-90

The specimens were divided into four groups. The first group, control, included two beams, one with internal shear reinforcement and one without internal shear reinforcement. These two beams will be used as a benchmark. Group A included three specimens without internal shear reinforcement. The three specimens were strengthened in shear with CFRCM (i.e., with a cementitious matrix). Specimens NS-C1-90 and NS-C2-90 were strengthened with one and two layers of CFRCM, respectively, in the vertical direction (i.e., at an angle of inclination of 90^o with respect to the longitudinal axis of the beam). Specimen NS-C2-0/90 was strengthened with two layers of CFRCM; one layer had a fabric aligned in the vertical direction at an angle of inclination of 90^o whereas the fabric of the other layer was aligned in the horizontal direction at an angle of inclination of 0^o with respect to the longitudinal axis of the beam. Group B consisted of three specimens with internal shear reinforcement. The three specimens were strengthened in shear using same CFRCM schemes as those of their counterparts from Group A. Group C included two specimens strengthened in shear with one layer of CFRGM (i.e., with a geopolymeric

matrix) aligned in the vertical direction at an angle of inclination of 90^o with respect to the longitudinal axis of the beam. One specimen had internal shear reinforcement whereas the other one did not include internal shear reinforcement.

3.3 Details of Test Specimens

Details of the specimens with and without internal shear reinforcement are shown in Figures 3.1 and 3.2, respectively. The specimens were 3300 mm long, 150 mm wide, and 500 mm deep. The longitudinal reinforcement consisted of 4 ϕ 25 mm in the tension side and 2 ϕ 25 in the compression side. The internal shear reinforcement, if existed, consisted of ϕ 5 mm stirrups at a spacing of 80 mm in both vertical and horizontal directions. The longitudinal tension steel reinforcing bars were located at an effective depth of d = 450 mm measured from the compression face of the beam. The compression steel reinforcing bars were located at a depth of d' = 25 mm. The concrete cover was 25 mm from all sides of the beams. the longitudinal reinforcement was extended beyond the support for a distance of 200 mm distance to avoid anchorage failure.

The internal shear reinforcement satisfies the ACI code provisions [1] for the minimum shear reinforcement. According to the ACI code [1], the spacing of distributed shear reinforcement shall not exceed the lesser of $d/5$. The area of the vertical shear reinforcement, A_v, shall not be less than a minimum value of $A_{v,min} = 0.0025\, b_w\, s_1$, where b_w is the width of the beam web and s_1 is the spacing between the vertical shear reinforcement. Also, the area of the horizontal shear reinforcement, A_h, shall less than a minimum value of $A_{h,min} = 0.0025\, b_w\, s_2$, where s_2 is the spacing between the horizontal shear reinforcement. in other words, the shear reinforcement ratio in the vertical direction, ρ_v, and in the horizontal direction, ρ_h, shall not be less

than 0.0025. The following calculation compares the internal shear reinforcement provide in the specimens to the minimum shear reinforcement requirements of the ACI code [1].

$s_{max} = d/5 = 450/5 = 90$ mm

$A_v = A_h = 2\pi d^2/4 = 2\pi 5^2/4 = 39.27\ mm^2$

$A_{v,min} = A_{h,min} = 0.0025 b_w s = (0.0025)(150)(80) = 30\ mm^2$

$$\rho_v = \rho_h = \frac{39.27}{(150)(80)} = 0.0033 > 0.0025$$

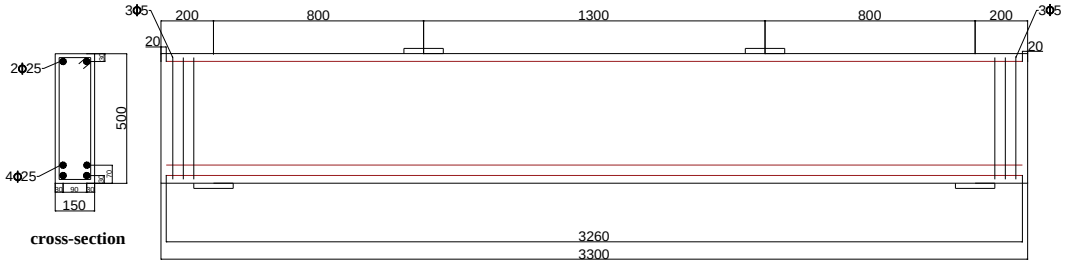

Figure 3.1: Details of a typical specimen without internal shear reinforcement (dimensions in mm)

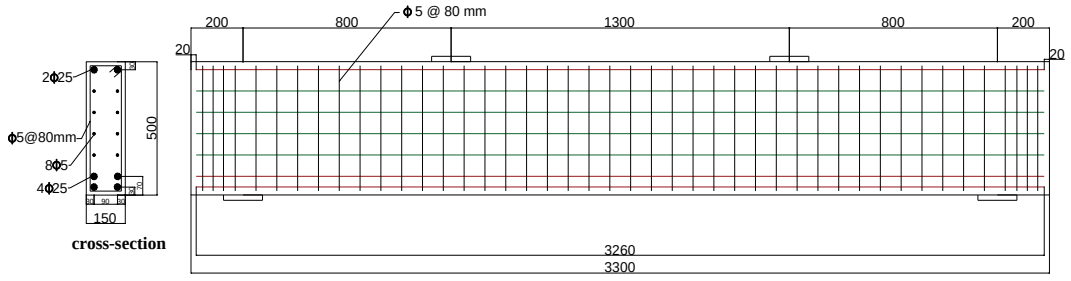

Figure 3.2: Details of a typical specimen with internal shear reinforcement (dimensions in mm)

3.4 Material Properties

3.4.1 Concrete

Ready-mix concrete was used to cast test specimens. The concrete mix proportions per cubic meter are given in Table 3.2. Ordinary Portland cement (OPC) was used in the mixes. The water-cement ratio (*w/c*) for concrete were 0.55. The coarse aggregate was a mix of 10 mm (33%) and 20 mm (67%) crushed aggregates. The fine aggregate was a blend of dune sand (37%) and 5 mm crushed aggregates (63%).

Table 3.2: Mix proportions for concrete

Material	Wight per 1 m3
OPC - Emirates Cement Factory	300 kg/m^3
20 mm Crushed - Al Buraimi Crusher (AI Ain)	700 kg/m^3
10 mm Crushed - Al Buraimi Crusher (AI Ain)	350 kg/m^3
05 mm Crushed - Stevin Rock (R.A.K.)	600 kg/m^3
Dune Sand - Al Ain Municipality (Al Ain)	350 kg/m^3
Free Water	165 I/m^3
Absorption	14 I/m^3
Total Water	179 I/m^3
Pozzolith LDIOE Added @ plant 1.00 to	2.00 I/m^3

Ten cylinders (150 x 300 mm) and five cubes (150 x 150 x 150 mm) were sampled from the concrete during casting. Five cylinders were used to determine the concrete compressive strength, while the other five cylinders were used to determine the splitting strength of the concrete. The five cubes were used to determine the concrete cube compressive strength. Figure 3.3 shows concrete samples during testing. Table 3.3 shows results of the concrete strength tests. The average cube and

cylinder compressive strengths of the concrete were 33.5 MPa and 26.3 MPa, respectively, whereas the splitting strength was on average 2.3 MPa.

A. B. C.

Figure 3.3: Concrete samples during testing: A. Cylinders comrpesion test, B. Splitting test, C. Cube comrpesion test

Table 3.3: Results of concrete strength tests

	Cube compressive strength (MPa)	Cylinder compressive strength (MPa)	Splitting strength (MPa)
Sample 1	32.0	28.9	2.1
Sample 2	32.7	25.5	2.5
Sample 3	34.4	23.4	2.2
Sample 4	33.8	28.3	2.5
Sample 5	34.4	25.5	2.4
Average	33.5	26.3	2.3

3.4.2 Steel Reinforcement

Steel reinforcing bars with a diameter of 25 mm were used for the longitudinal reinforcement, and 5 mm diameter bars were used for the internal shear reinforcement. The 25 mm bars have ribs to improve the bond between the bars and the concrete. For the 5 mm bars, it was smooth without ribs. Table 3.4 shows measured properties of the steel reinforcing bars. The average yield strengths for the 25 mm and 5 mm

diameter bars were 539 MPa and 505 MPa, respectively, whereas their respective ultimate tensile strengths were 649 MPa and 543 MPa, respectively.

Table 3.4: Properties of steel bars

Sample No.	Nominal Diameter (mm)	Nominal Cross-Sectional Area (mm^2)	Yield Strength (MPa)	Tensile Strength (MPa)
1	25	491	555	668
2	25	491	535	643
3	25	491	527	635
4	5	19.6	499	534
5	5	19.6	511	552

3.4.3 FRCM

The carbon fabric used in the current study was unidirectional (Figure 3.4). properties of the fabrics provided by the manufacturer are given in Table 3.5. The measured width and thickness of one fiber bundle were approximately 5.0 mm and 0.54 mm, respectively. This corresponds to a cross-sectional area per unit length of 159 mm^2/m, which is consistent with that provided by the manufacturer (157 mm^2/m).

Figure 3.4: Fibers mesh

Table 3.5: Carbon-fiber mesh properties (provided by the manufacturer [14])

Property	Carbon
Weight per unit area (g/m^2)	281
Tensile strength (MPa)	4,300
Modulus of elasticity (GPa)	240
Elongation at break (%)	1.8
Cross-sectional area per unit length (mm^2/m)	157

3.4.4 Cementitious Mortar

The cementitious mortar provided by the manufacturer is a polymer-modified mortar based on organic binders, polymer fibers, and selected aggregates. The mortar was mixed as per the procedure provide by the manufacturer. Based on results of fiver replicate samples, the cementitious matrix provided by the manufacturer had an average 28-day cube compressive strength of 42 MPa, cylinder compressive strength of 35 MPa, splitting tensile strength of 2.4 MPa, and young's modulus of 29 GPa. respectively.

3.4.5 Geopolymer Mortar

The geopolymeric matrix included slag (GGBS) and fly ash as binding materials, dune sand as fine aggregates, and an alkaline activator solution consisting of sodium silicate (SS) and sodium hydroxide (SH). Proportions and components of the geopolymeric matrix are given in Table 3.6. The geopolymeric matrix had an average measured 28-day cube compressive strength of 43 MPa, cylinder compressive strength of 34 MPa, splitting tensile strength of 3.0 MPa, and young's modulus of 7 GPa.

Table 3.6: Geopolymeric matrix components and proportions

Mixture proportion (kg/m^3)				
Fly ash	Slag	Dune sand	Sodium silicate (SS)	Sodium hydroxide (SH)
362.5	362.5	752	285.5	114

3.5 Specimens Fabrication

3.5.1 Reinforcing Cages and Formwork

First, the longitudinal reinforcements and longitudinal stirrups cut to the designed length. Then, the stirrups cut and bent. After that, the reinforcing cages fabricated to the required design, as shown in Figures 3.5 and 3.6. Ten wooden formworks boxes were fabricated using 18 mm thick plywood sheets. Each formwork was surrounded by rigid timber to provide a lateral failure during casting. Figure 3.7 shows the formworks.

Figure 3.5: Steel cages of the beams with stirrups

Figure 3.6: Steel cages of the beams without stirrups

Figure 3.7: Formwork of the beams

3.5.2 Steel Strain Gauges

Strain gauges with a 5 mm gauge length were bonded to the surface of the longitudinal steel reinforcement at discrete locations in the shear span to record the steel strain profile as shown in Figure 3.8. For the beams with internal shear reinforcement, two additional strain gauges, 5 mm long each, were installed on the shear reinforcement in the mid of each shear span; one was bonded to a horizontal bar and the other one was bonded to a vertical stirrup, as shown in Figure 3.9. Prior to installation of the strain gauges, the ribs of the steel bars at location of the strain gauge were removed using a grinder and surface of the steel was then cleaned using an alcohol solution. The strain gauge was then bonded to the surface of the steel bar using an adhesive. An isolated tape was then installed on top of the bonded strain gauge. Finally, the area was wrapped with electrical tape for the purpose of protection. The materials used along with a photograph taken during installation of the strain gauges are show in Figure 3.10.

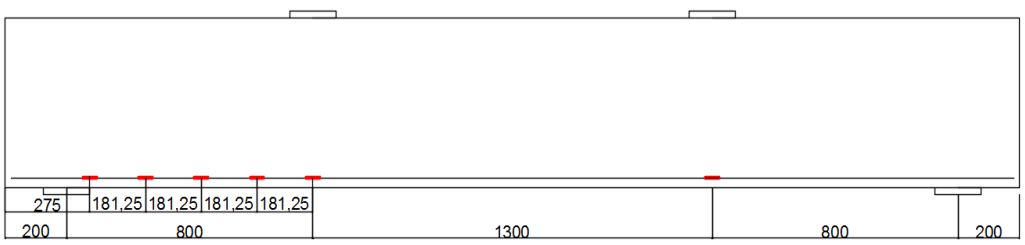

Figure 3.8: Locations of longitudinal steel strain gauges

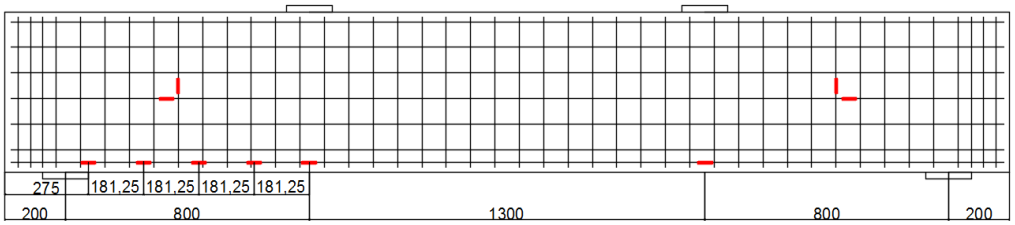

Figure 3.9: Locations of steel strain gauges on internal shear reinforcement

A. B.

Figure 3.10: Installation of strain gauges: A. Materials used, B. Bonding strain gauges to steel bars

3.5.3 Concrete Casting

The steel cages were installed inside the formwork before casting the concrete. Mortar biscuits with a thickness of 15 mm were used to obtain the concrete cover during casting. Steel hooks were installed to help during the movement and handling of the beams. A ready-mix company supplied the concrete. During the casting, an electrical vibrator was used to improve the concrete consolidation and avoid the formation of voids. Figure 3.11 shows steel cages inside the formwork whereas Figure 3.12 shows the placement of the ready-mix concrete inside he forms. After the concrete casting, the surface of the specimen was leveled using a trowel. Then, the beams were covered with burlap and a plastic sheet for 24 hrs to maintain moisture. The beams were then subjected to curing using periodically wetted burlaps for 28

days. The cylinder and cube concrete samples were subjected to the same curing system. Figure 3.13 shows concrete beams during finishing the surface and during curing.

Figure 3.11: Steel cages inside the forms

A. B. C.

Figure 3.12: Concrete casting: A. Ready-mix concrete truck, B. Placement of concrete, C. Vibration of concrete

A. B. C.

Figure 3.13: Finsising and curing: A. Leveling the concrete surface, B. Beams covered with burlaps, C. Spraying water for curing

3.5.4 FRCM/FRGM Strengthening

Shear strengthening included cutting of the fabric, preparation of the concrete surface, mixing of the matrix, application and curing of FRCM/FRGM composites. The fabric was first cut to the desired length as shown in Figure 3.14 then instrumented with strain gauges at locations coincide with the mid of the shear span. The surface of the fabric was first prepared by applying a thin layer of adhesive that was left to dry for 24 hr. The surface was then cleaned then the strain gauge was installed following same procedure adopted when installed on the steel reinforcing bars (Figures 3.15).

A. B.

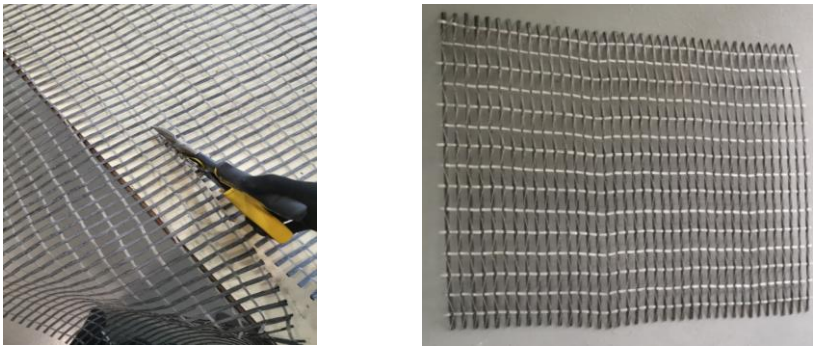

Figure 3.14: Prepartion of fabrics: A. Cutting the fabric mesh, B. Prepared carbon fabric

A. B.

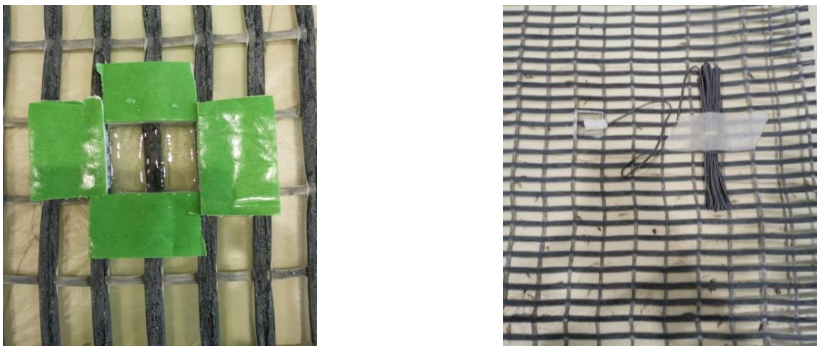

Figure 3.15: Installing the stain gauges on the fiber: A. An adhesive on the fabric for surface preparation, B. Fabric with a strain gauge installed

The concrete surface was roughened using a high-pressurized water jet (Figure 3.16). The surface was then left to dry prior to the application of the composites. The cementitious mortar was prepared following the procedure provided by the manufacture (Figure 3.17). One layer of mortar with a thickness of approximately 4 mm was first applied on the roughened concrete surface. The carbon fabrics were then placed on top of the mortar layer then fully impregnated in the mortar using hand pressure. A second layer of mortar, with a thickness of approximately 4 mm, was then applied on top of the fabric. Same procedure was adopted in case additional layers of composites were installed. Figure 3.18 shows the steps of FRCM application. The strengthening composite layers were cured for 28 days using periodically wetted burlap sheets as shown in Figure 3.19.

A. B.

Figure 3.16: Concrete surface prepartion: A. Use of water jet for surface preparation, B. Concrete after surface roughening

A. B.

Figure 3.17: Preparation of the cementitious mortar: A. Solid cementitious material, B. Mixing of mortar

A. B.

C. D.

Figure 3.18: Application of FRCM composites: A. Application of first layer of mortar, B. Placement and impregnation of the fabric, C. Application of the second layer of mortar, D. Leveling of the concrete surface

A. B.

Figure 3.19: Curing of of FRCM composites: A. Beams covered with burlaps, B. Spraying water on the burlaps

Shear strengthening with geopolymeric-based FRGM composites followed the same procedure adopted for FRCM strengthening. The difference was in the preparation of the matrix. Also, no water-curing was required. The solid materials of the geopolymeric matrix were placed in a container, and the alkaline activator solution was placed in another container. The solid materials were then mixed with the alkaline solution to produce the geopolymeric matrix. Figure 3.20 shows how the

geopolymeric matrix was prepared whereas Figure 3.21 summarizes FRGM application.

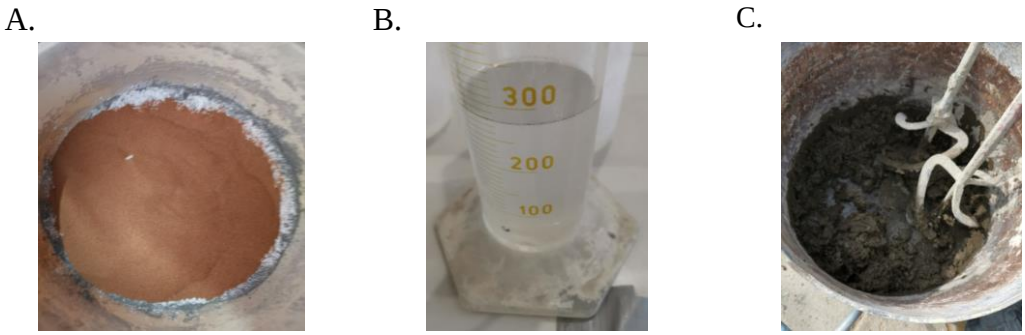

Figure 3.20: Preparation of the geopolymeric matrix: A. Solid materials, B. Alkaline activator solution, C. Geopolymeric mixture

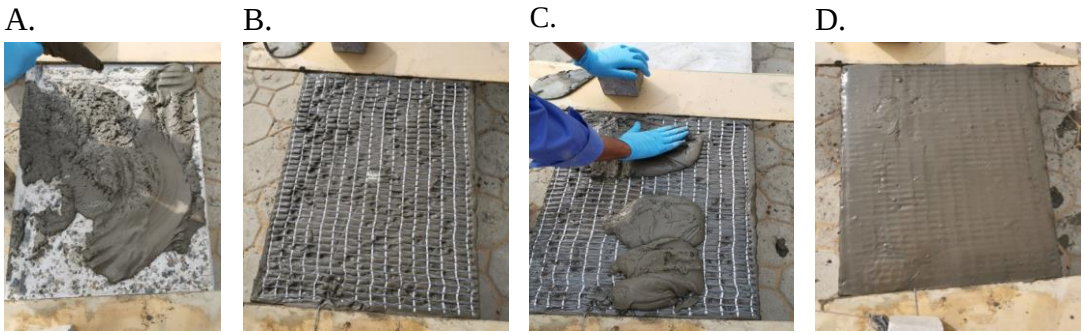

Figure 3.21: Application of FRGM composites: A. First layer of geopolymer, B. Impregnation of fabric, C. Second layer of geopolymer, D. Finished surface

3.6 Instrumentation and Testing

All the deep beams were tested under four-point bending until failure. The beams were placed on two supports that were 2900 mm apart from each other. The load was applied on two points that were 1300 mm apart at the top by using two 500 kN actuators. The experiments were performed under load control at a rate of 0.5 kN/sec then, the load scheme was changed to be under a displacement control at a rate of 0.6 mm/min at about 85% - 90% of the theoretical load capacity. Changing the loading scheme to be a displacement-controlled was done for safety reasons to prevent

the catastrophic failure of the beam at the ultimate load. Four steel plates, 150 x 150 x 20 mm each, were located under the load points and above the supports to prevent concentration of stresses. Two load cells with 500 kN capacity were placed between the actuators and the top plates to record the applied load. Three linear variable differential transducers (LVDTs) were located at the mid-span under the beam and under the support to record the net deflection. Concrete strain gauges with a 60 mm gauge length were bonded to the concrete surface at specific locations to determine the concrete stains, as shown in Figure 3.22. The load cells, LVDTs, and strain gauges, were linked to one data acquisition system to record all the readings at the same time. Figure 3.23 shows the test setup whereas a test in progress is shown in Figure 3.24.

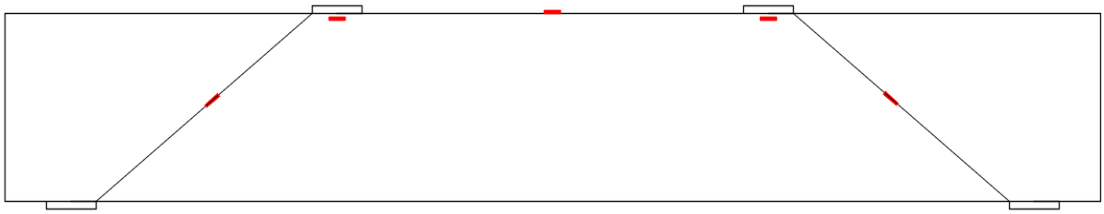

Figure 3.22: Positions of concrete strain gauges positions

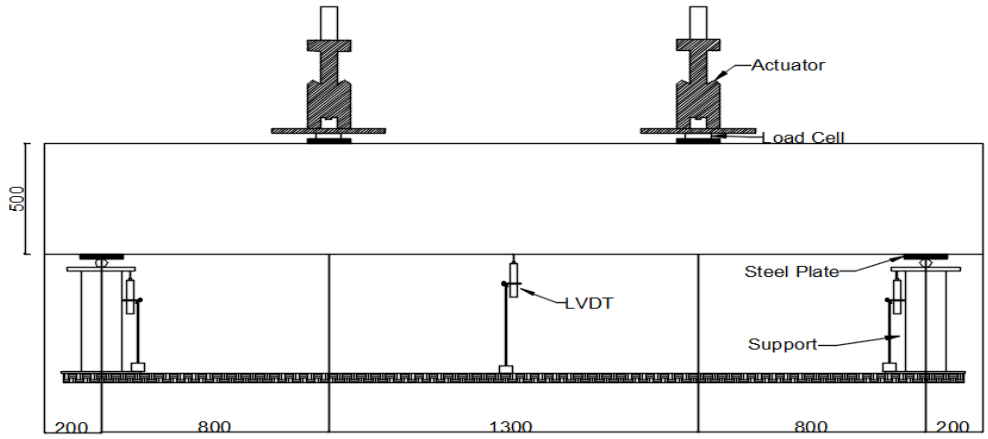

Figure 3.23: Test setup

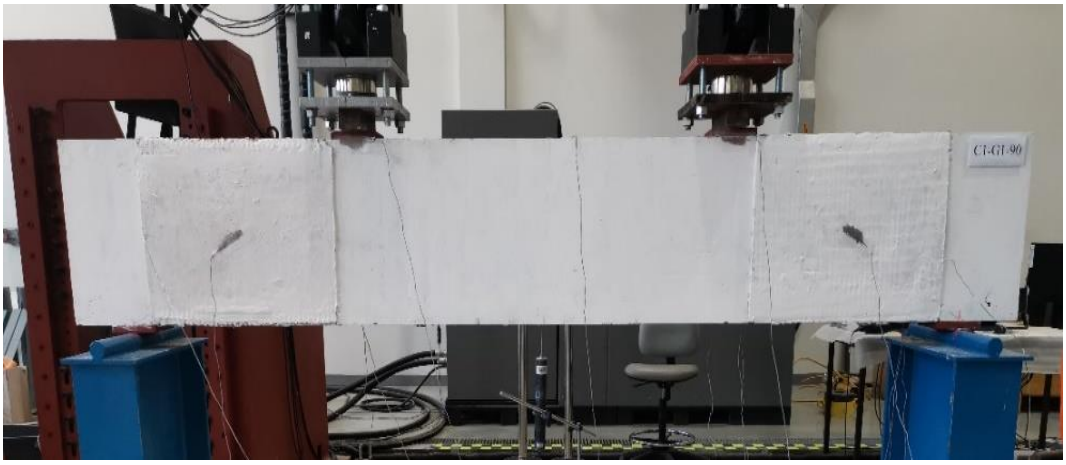

Figure 3.24: A test in progress

3.7 Summary

This chapter introduced details of specimens' fabrication and procedure of testing of ten large-scale RC deep beam specimens with an *a/h* of 1.6 to failure in a four-point bending configuration. Also, the test matrix, material parameters, test setup, and instruments were provided. Experimental test results and outcomes are presented and discussed in the following chapter.

Chapter 4 : Experimental Results

4.1 Introduction

This chapter presents experimental results of the tests conducted in the current study. The results include shear load-deflection response, failure mode, and strain measurements. The effectiveness of using FRCM/FRGM to improve the shear response of RC deep beams with and without internal shear reinforcement is elucidated.

4.2 Shear Load-Deflection Response

The shear load-deflection relationships of the tested beams are shown in Figure 4.1 to Figure 4.4. The shear load values represent the support reaction. The deflection represents the net midspan deflection calculated by subtracting the average deflection measured under the two supports from measured midspan deflection.

4.2.1 Control Un-strengthened Specimens

Figure 4.1 shows the shear load-midspan deflection response of the un-strengthened specimens Control-NS and Control-ST. Specimen Control-NS did not include internal shear reinforcement whereas specimen Control-ST had internal shear reinforcement. Test results of the control un-strengthened specimens are summarized in Table 4.1. The shear load-deflection response for the Control-NS beam started with a linear relationship between the load and the deflection until the load reached an approximate value of 104 kN where a small drop in load happened due to initiation of the first shear crack. In the post-cracking stage, the deflection continued to increase but at a higher rate. Another drop in load was observed at a load value of 113 kN due

to initiation of another shear crack near the support. The beam failed at a maximum shear load of 139 kN and corresponding deflection of 6.8 mm. Specimen Control-ST exhibited a quasilinear shear load-deflection response until it reached its maximum shear load capacity of 348 kN at a midspan deflection 11.7 mm. Although the first shear crack initiated at an approximate load value of 176 kN, no significant change in the slope of the shear load-deflection response was observed at the onset of shear cracking due to the presence of internal shear reinforcement.

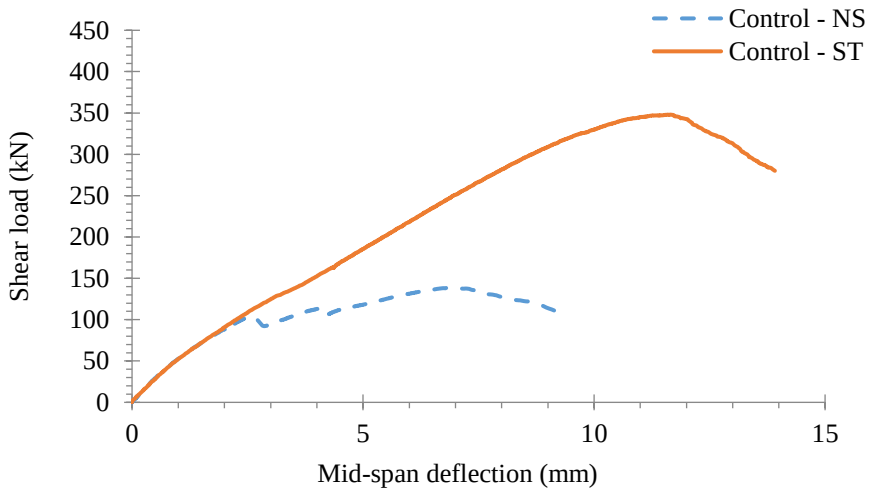

Figure 4.1: Shear load-deflection response of the control specimens

Table 4.1: Test results of the control un-strengthened specimens

Group	Specimen	Shear cracking stage		Ultimate stage	
		V_{cr} (kN)	Δ_{cr} (mm)	V_{max} (kN)	Δ_{peak} (mm)
Control	Control-NS	104	2.6	139	6.8
	Control-ST	176	4.7	348	11.7

4.2.2 Strengthened Specimens of Group A

Figure 4.2 shows the shear load-deflection response of specimens of group A, namely, NS-C1-90, NS-C2-90, NS-C2-0/90 strengthened with FRCM (i.e., with a

cementitious matrix). Table 4.2 summaries the corresponding test results. Results of the specimen Control-NS is included for the reason of comparison. Specimens of group A did not include internal shear reinforcement. It can be seen that the pre-cracking stiffness of the strengthened specimens almost coincided with that of the control specimen. Strengthened specimens exhibited first shear cracking at a load value in the range of 150 kN to 160 kN. Following shear cracking, the deflection of the strengthened specimens continued to increase almost linearly until the beams reached their shear capacity. Shear strengthening with one layer of FRCM increased the shear capacity by 95%. Increasing the number of FRCM layers had almost no effect on the stiffness of the strengthened specimens. Nevertheless, the shear capacities of the specimens with two layers of FRCM was on average 8% higher than that of the specimens with one layer of FRCM. The shear capacities of specimens NS-C2-90 and NS-C2-0/90 were insignificantly different. Eventually, specimens NS-C1-90, NS-C2-90, and NS-C2-0/90 reached their shear capacity at respective load values of 271 kN, 290 kN, and 288 kN, and corresponding midspan deflections of 8.5 mm, 8.9 mm, and 9.7 mm, respectively.

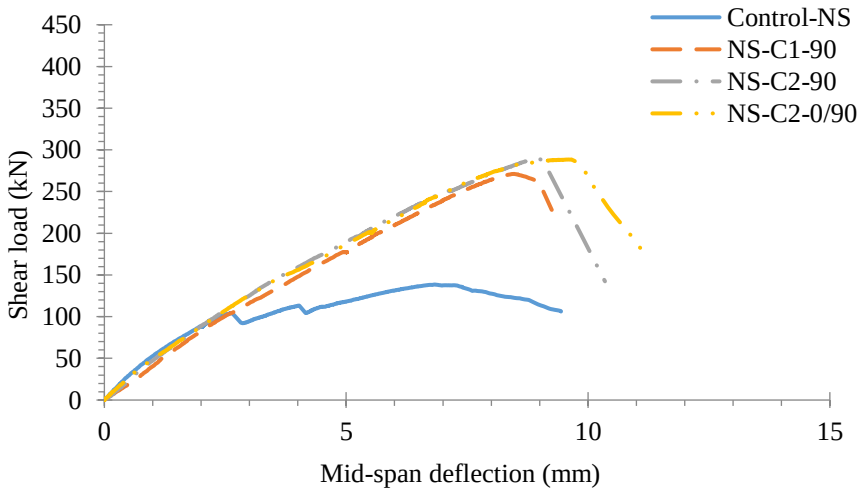

Figure 4.2: Shear load-deflection response of specimens of group A

Table 4.2: Test results of specimens of group A

Group	Specimen	Shear cracking stage		Ultimate stage	
		V_{cr} (kN)	Δ_{cr} (mm)	V_{max} (kN)	Δ_{peak} (mm)
Control	Control-NS	104	2.6	139	6.8
A	NS-C1-90	105	2.8	271	8.5
	NS-C2-90	150	3.7	290	8.9
	NS-C2-0/90	160	3.8	288	9.7

4.2.3 Strengthened Specimens of Group B

The shear load-deflection response of specimens of group B are plotted in Figure 4.3. The corresponding test results are summarized in Table 4.3. Results of the specimen Control-ST is included for the reason of comparison. Specimens of group B had internal shear reinforcement and strengthened with FRCM (i.e., with a cementitious matrix). The stiffness of the strengthened specimens was insignificantly different from that of Control-ST, except specimen ST-C2-90, which was slightly stiffer, possibly because it was strengthened with two layers of FRCM. The first crack appeared in specimens ST-C1-90, ST-C2-90, and ST-C2-0/90 beams at the load of 105 kN, 150 kN, and 155 kN, respectively. The shear capacities of the specimens ST-C1-90, ST-C2-90, and ST-C2-0/90 were 409 kN, 411 kN, and 377 kN, with respective shear strength gain of 18%, 18%, and 8%. The specimens reached their shear capacity at respective midspan deflections of 13.4 mm, 11.7 mm, and 12.2 mm.

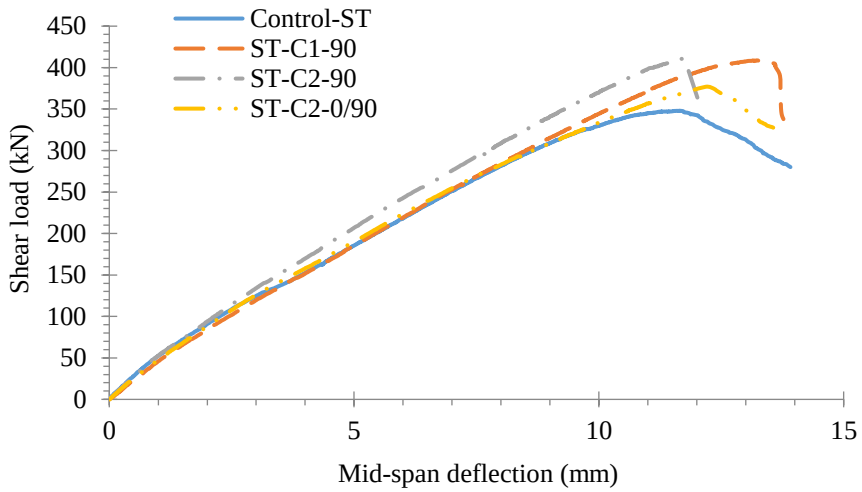

Figure 4.3: Shear load-deflection response for specimens of group B

Table 4.3: Test results of specimens of group B

Group	Specimen	Shear cracking stage		Ultimate stage	
		V_{cr} (kN)	Δ_{cr} (mm)	V_{max} (kN)	Δ_{peak} (mm)
Control	Control-ST	176	4.7	348	11.7
B	ST-C1-90	105	2.4	409	13.4
	ST-C2-90	150	3.5	411	11.7
	ST-C2-0/90	155	3.9	377	12.2

4.2.4 Strengthened Specimens of Group C

Figure 4.4 presents the shear load-deflection response of specimens NS-G1-90 and ST-G1-90 which were strengthened with FRGM (i.e., with a geopolymeric matrix). The corresponding test results are summarized in Table 4.4. Results of the benchmark specimens Control-NS and Control-ST are also included to compare their response with those of their counterparts strengthened with FRGM. Shear cracks developed in strengthened specimens NS-G1-90 and ST-G1-90 were not visible during testing. The invisibility of cracks on the surface could be attributed to the low young's modulus of the geopolymeric matrix, which may have facilitated large deformation of the matrix without visible cracks on the surface. Strengthened

specimens exhibited a quasilinear response with an insignificant change in the slope of the shear load-deflection response. Specimens with internal shear reinforcement, Control-ST and ST-G1-90, exhibited higher shear capacity and higher deformation capacity than those of their respective counterparts, Control-NS and NS-G1-90, that did not include stirrups. In the absence of internal shear reinforcement, the response of the strengthened specimen NS-G1-90 outperformed that of its counterpart Control-NS (77% strength gain was recorded). The improvement in the shear response caused by the FRGM shear strengthening system was less pronounced in the presence on internal shear reinforcement. Specimen ST-G1-90 failed at a shear capacity of 380 kN, which was 8% higher than that of its counterpart specimen Control-ST. The strengthened specimens NS-G1-90 and ST-G1-90 reached their shear capacities of 246 kN and 380 kN at midspan deflections of 7.7 mm and 11.4 mm, respectively.

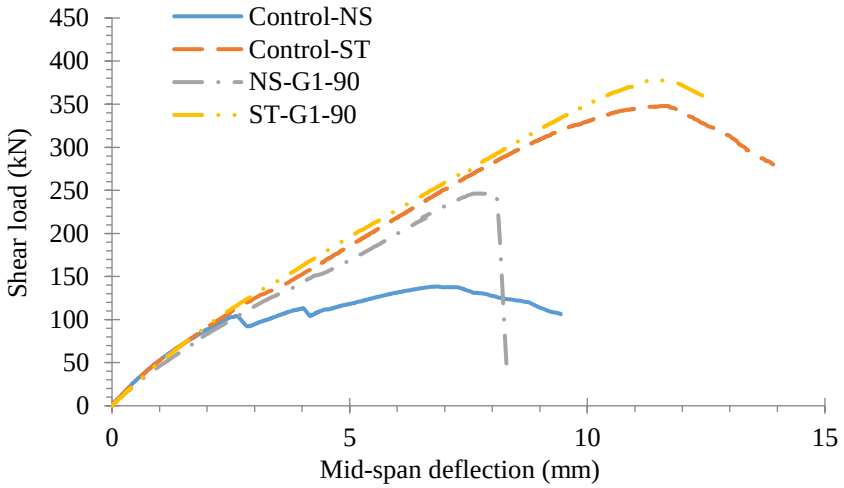

Figure 4.4: Shear load-deflection response for specimens of group C

Table 4.4: Test results of specimens of group C

Group	Specimen	Shear cracking stage		Ultimate stage	
		V_{cr} (kN)	Δ_{cr} (mm)	V_{max} (kN)	Δ_{peak} (mm)
Control	Control-NS	104	2.6	139	6.8
	Control-ST	176	4.7	348	11.7
C	NS-G1-90	-	-	246	7.7
	ST-G1-90	-	-	380	11.4

4.3 Crack Pattern and Failure Mode

4.3.1 Un-strengthened Specimens

The crack pattern at failure for specimen Control-NS is shown in Figure 4.5. Initially, the beam exhibited a diagonal crack initiated at the mid of each shear span. As the load progressed, the cracks propagated rapidly toward the support and load points. In the meantime, the beam exhibited large deformations with insignificant increase in load. The beam failed in a shear-compression mode of failure when the diagonal crack penetrated into the compression zone, which caused concrete crushing at the tip of the crack. The crack pattern at failure for specimen Control-ST is shown in Figure 4.6. The first shear crack appeared diagonally in the mid of the shear span. As the load increased, additional cracks developed in the diagonal direction. Further increase in load resulted in propagation of cracks toward the support and load points in addition to formation of additional parallel cracks in the diagonal direction. The parallel diagonal cracks formed a diagonal strut. The beam eventually failed by crushing of the concrete along the diagonal strut.

A.

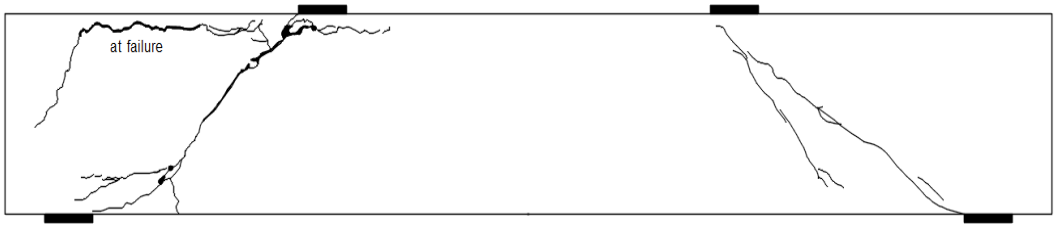

B.

C.

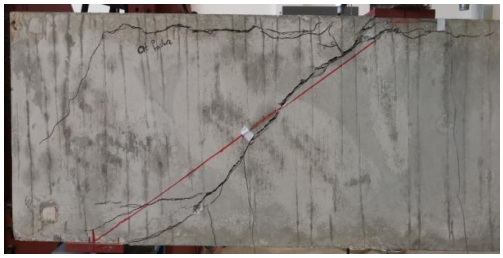

Figure 4.5: Crack pattern of specimen Control-NS: A. Schematic drawing of the crack pattern, B. Picture of the beam at failure, C. Close view of the crack pattern (west shear span)

A.

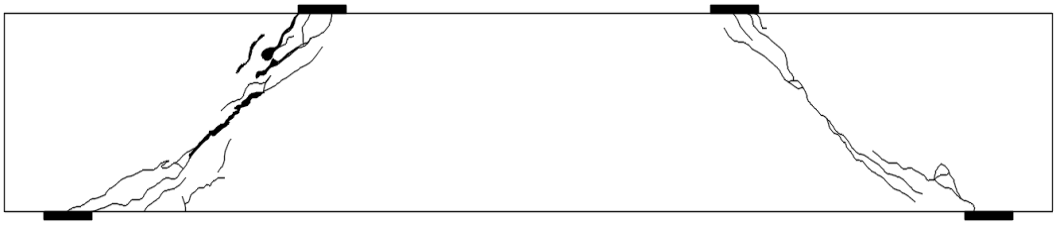

B.

C.

Figure 4.6: Crack pattern of specimen Control-ST: A. Schematic drawing of the crack pattern, B. Picture of the beam at failure, C. Close view of the crack pattern (west shear span)

4.3.2 Strengthened Specimens of Group A

Figure 4.7 shows the crack pattern of specimen NS-C1-90 at failure. A diagonal shear crack developed in the mid of the shear span then propagated toward the support and load points. The beam failed due to crushing of the concrete at the top part of the diagonal strut (i.e., diagonal compression mode of failure). The crack pattern of specimens NS-C2-90 and NS-C2-0/90 at failure are shown in Figures 4.8 and 4.9, respectively. The beams exhibited multiple cracks in the shear span during the test. They eventually failed due to crushing of the diagonal strut developed in the shear spans.

A.

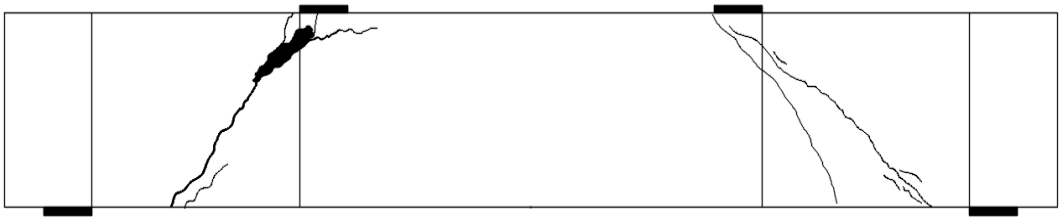

B.

C.

Figure 4.7: Crack pattern of specimen NS-C1-90: A. Schematic drawing of the crack pattern, B. Picture of the beam at failure, C. Close view of the crack pattern (west shear span)

A.

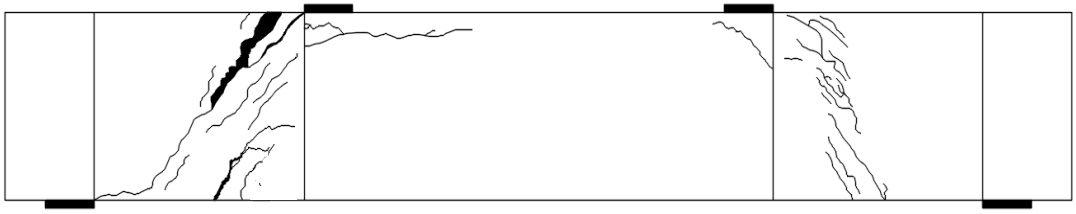

B.

C.

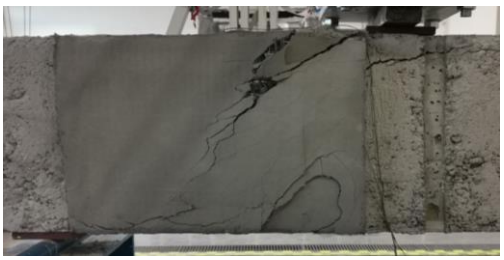

Figure 4.8: Crack pattern of specimen NS-C2-90: A. Schematic drawing of the crack pattern, B. Picture of the beam at failure, C. Close view of the crack pattern (west shear span)

A.

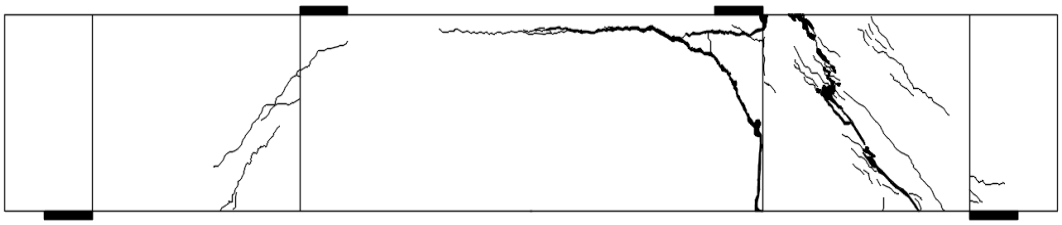

B.

C.

Figure 4.9: Crack pattern of specimen NS-C2-0/90: A. Schematic drawing of the crack pattern, B. Picture of the beam at failure, C. Close view of the crack pattern (east shear span)

4.3.3 Strengthened Specimens of Group B

The crack patterns at failure of specimens ST-C1-90, ST-C2-90, and ST-C2-0/90 are presented in Figures 4.10, 4.11, and 4.12, respectively. Specimen ST-C1-90 exhibited multiple shear cracks in the shear spans. Specimen ST-C2-90 with two layers of FRCM in the vertical direction exhibited an increased amount of shear cracks in the shear span (i.e., band of shear cracks) relative to those experienced by the other two specimens. All specimens of this group failed by crushing of the diagonal strut in the shear span. Crushing of concrete was evident in the middle of the diagonal strut of

specimens ST-C1-90 and ST-C2-90 whereas ST-C2-0/90 experienced concrete crushing at the top part of the diagonal strut in the shear span.

A.

B.

C.

Figure 4.10: Crack pattern of specimen ST-C1-90: A. Schematic drawing of the crack pattern, B. Picture of the beam at failure, C. Close view of the crack pattern (east shear span)

A.

B.

C.

Figure 4.11: Crack pattern of specimen ST-C2-90: A. Schematic drawing of the crack pattern, B. Picture of the beam at failure, C. Close view of the crack pattern (east shear span)

A.

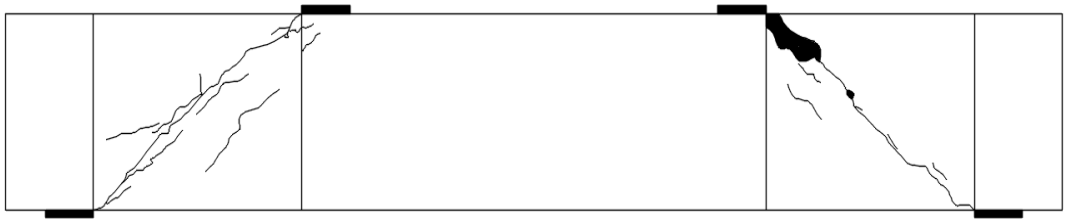

B.

C.

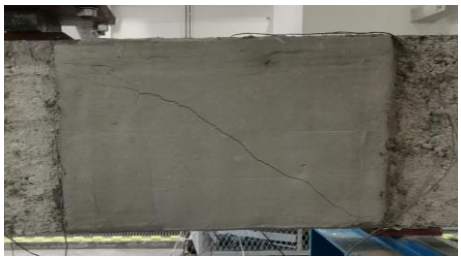

Figure 4.12: Crack pattern of specimen ST-C2-0/90: A. Schematic drawing of the crack pattern, B. Picture of the beam at failure, C. Close view of the crack pattern (east shear span)

4.3.4 Strengthened Specimens of Group C

The crack pattern of specimens NS-G1-90 and ST-G1-90 are shown in Figure 4.13 and 4.15, respectively. Both specimens were strengthened FRGM (i.e. with a geopolymeric matrix). The cracks were not visible during testing. The low young's modulus of the geopolymeric matrix could have facilitated large deformation in the matrix and prevented cracks from being visible on the surface of the matrix. Specimen NS-G1-90 failed suddenly due to crushing of the diagonal strut in the east shear span.

Specimen ST-G1-90 experienced also crushing of the diagonal strut in the middle of the west shear span.

A.

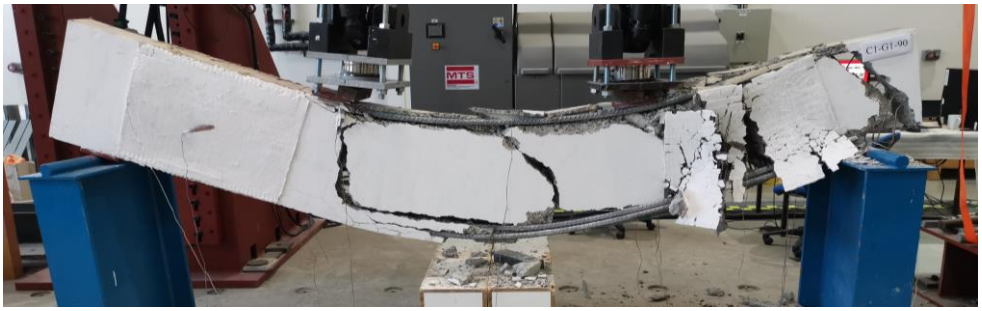

B.

Figure 4.13: Crack pattern of specimen NS-G1-90: A. Picture of the beam at failure, B. Close views at failure (east shear span)

A.

B.

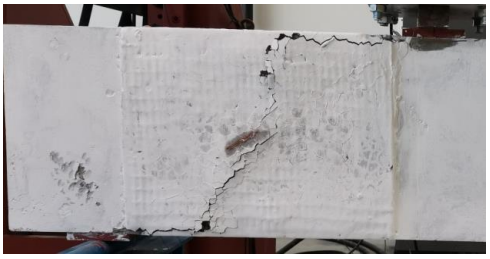

Figure 4.14: Crack pattern of specimen ST-G1-90: A. Picture of the beam at failure, B. Close views of the crack pattern (west shear span)

4.4 Performance Evaluation

A summary of the main results of all tested beams is shown in Table 4.5. The control specimen that did not include internal shear reinforcement exhibited shear cracking at approximately 75% of the shear capacity (i.e., $V_{cr}/V_{max} = 0.75$). The beams failed shortly after initiation of shear cracks in a shear-compression mode of failure because of the absence of internal shear reinforcement. The inclusion of internal shear reinforcement changed the mode of failure to crushing of the concrete strut (i.e., diagonal compression), increased the shear cracking load, and improved the shear capacity. The presence of internal shear reinforcement also increased the difference between the cracking and ultimate load, and thus, reduced the ratio V_{cr}/V_{max} to 0.51. The shear capacity of specimen Control-ST having internal stirrups was 1.6 times that of its counterpart Control-NS without stirrups.

Results of specimens of group A indicate that FRCM in RC deep beams can play a role similar to that of the internal shear reinforcement. Specimens of group A exhibited a reduced ratio of V_{cr}/V_{max}, higher shear capacity, and higher deformation capacity than those of their counterpart specimen Control-NS. Also, shear strengthening with FRCM changed the mode of failure to a diagonal compression mode of failure (i.e., crushing of the diagonal concrete strut). Specimen NS-C1-90, with one layer of FRCM, exhibited a shear strength gain of 95%. Increasing the number of FRCM layers insignificantly increased the shear capacity. The shear capacity of specimens NS-C2-90 and NS-C2-0/90, with two layers of FRCM, was on average 8% higher than that of specimen NS-C1-90. The angle of orientation of the second layer of FRCM had an almost no effect on the shear capacity of the specimens

without internal stirrups. Specimens NS-C2-90 and NS-C2-0/90 exhibited shear strength gains of 109% and 107%, respectively.

Results of specimens of group B indicate that the effectiveness FRCM to improve the shear capacity of RC deep beam specimens is affected by the presence of internal shear reinforcement. The gain in shear capacity was less pronounced in the presence of internal shear reinforcement. Only 18% shear strength gain was recorded due to shear strengthening with one layer of FCRM aligned in the vertical direction. Increasing the amount of FRCM in the vertical direction did not result in an additional shear strength gain in the presence of internal shear reinforcement. This implied that specimens of this group were over-reinforced for shear, and the diagonal strut could have reached its maximum capacity. Positioning the second layer of carbon fabric in the horizontal direction (i.e., at angle of inclination of 0^o) tended to be less effective than placing it in the vertical direction (i.e., at angle of inclination of 90^o).

Results of specimens of group C demonstrate the viability of using a geopolymeric matrix as a sustainable alternative to commercial cementitious mortar. Specimen NS-G1-90 strengthened with one layer of FRGM (i.e., with a geopolymeric matrix) experienced 77% shear strength gain relative to that of its counterpart specimen Control-NS. The shear capacity of specimen NS-G1-90 was only 9% lower than that of its counterpart strengthened with FRCM (i.e., with a cementitious matrix). The effectiveness of the shear strengthening system involving a geopolymeric matrix was reduced in the presence of internal stirrups similar to the behavior of their counterpart specimens strengthened with FRCM (i.e., with a cementitious matrix). Only 9% shear strength gain was recorded for specimen ST-G1-90. The specimen failed by crushing of the diagonal strut. The shear capacity of specimen ST-G1-90

was only 7% lower than that of its counterpart ST-C1-90 strengthened with FRCM (i.e., with a cementitious matrix).

Table 4.5: Summary of test results

Group	Specimen	Shear cracking stage		Ultimate stage		V_{cr}/V_{max}	Strength gain* (%)	Failure mode
		V_{cr} (kN)	Δ_{cr} (mm)	V_{max} (kN)	Δ_{peak} (mm)			
Control	Control-NS	104	2.6	139	6.8	0.75	-	Shear compression
	Control-ST	176	4.7	348	11.7	0.51	-	Strut crushing
A	NS-C1-90	105	2.8	271	8.5	0.39	95	Strut crushing
	NS-C2-90	150	3.7	290	8.9	0.50	109	Strut crushing
	NS-C2-0/90	160	4.2	288	9.7	0.56	107	Strut crushing
B	ST-C1-90	105	2.4	409	13.3	0.26	18	Strut crushing
	ST-C2-90	150	3.5	411	11.7	0.36	18	Strut crushing
	ST-C2-0/90	155	3.9	377	12.2	0.41	8	Strut crushing
C	NS-G1-90	-	-	246	7.7	-	77	Strut crushing
	ST-G1-90	-	-	380	11.4	-	9	Strut crushing

*Strength gain is calculated relative to strength of the corresponding control specimen

4.5 Strain Measurements

4.5.1 Steel Strains

The strain in the main longitudinal steel reinforcement was measured at four points within the shear span. Figures 4.15 to 4.18 shows the measured steel strains in the shear span at four different loading stages: 25%, 50%, 75%, and 100% of the shear capacity. Some strain readings were missing due to damage of the strain before testing.

All specimens experienced an almost uniform steel strain profile within the shear span. This behavior confirms the development of the arch action in all of the tested specimens. The strains in all locations increased with an increase in the applied load. Eventually, all specimens reached their shear capacity at steel strain values less than the yield strain as planned in the design. Table 4.6 presents the maximum steel strain recorded at peak load for all of the tested specimens.

A.

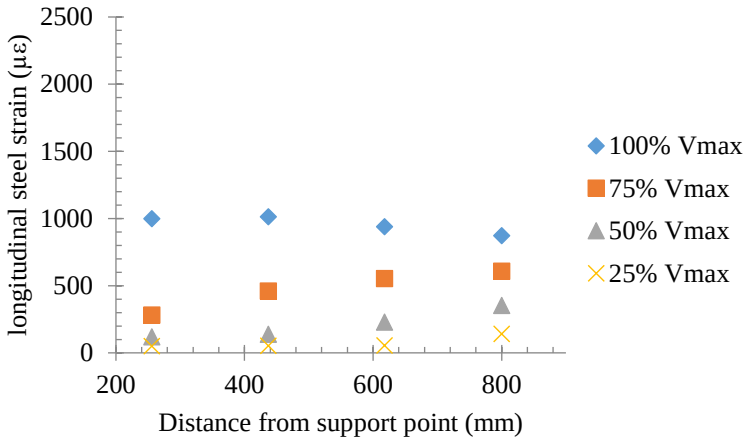

B.

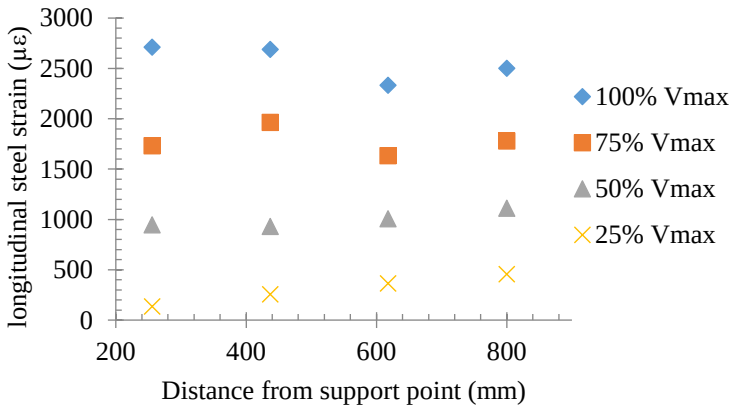

Figure 4.15: Steel strain profile of un-strengthened specimens: A. Specimen Control - NS, B. Specimen Control – ST

A.

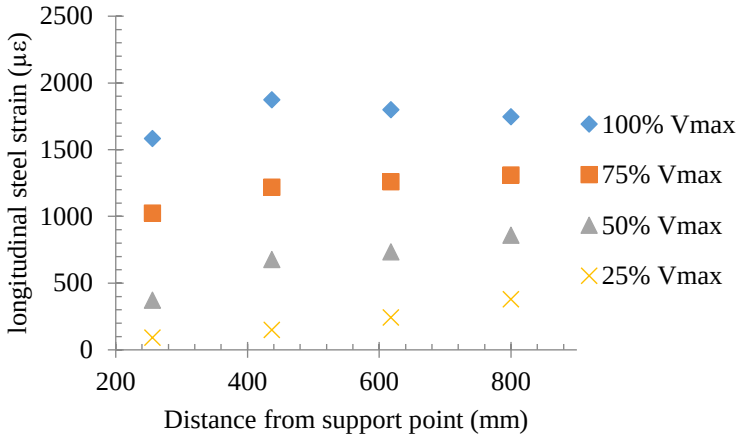

B.

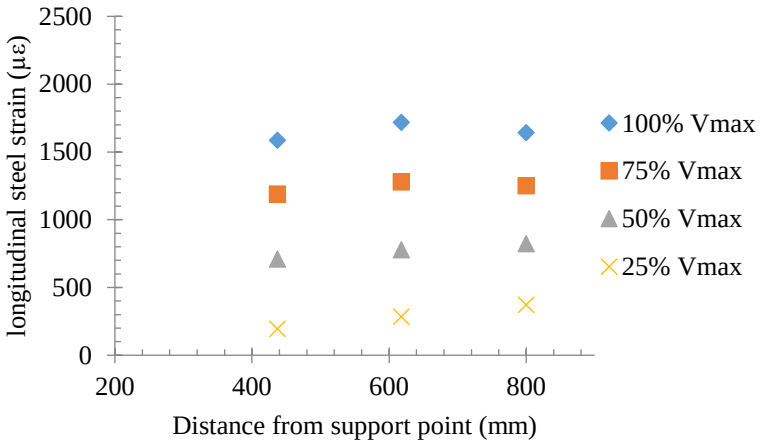

Figure 4.16: Steel strain profile of specimens of group A: A. Specimen NS-C2-90, B. Specimen NS-C2-0/90

A.

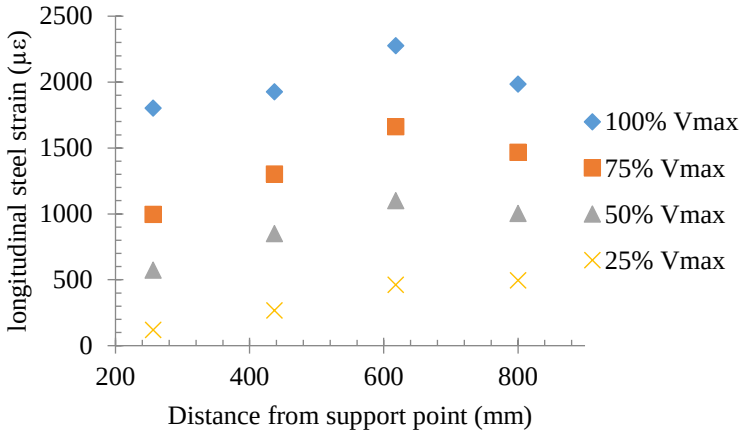

B.

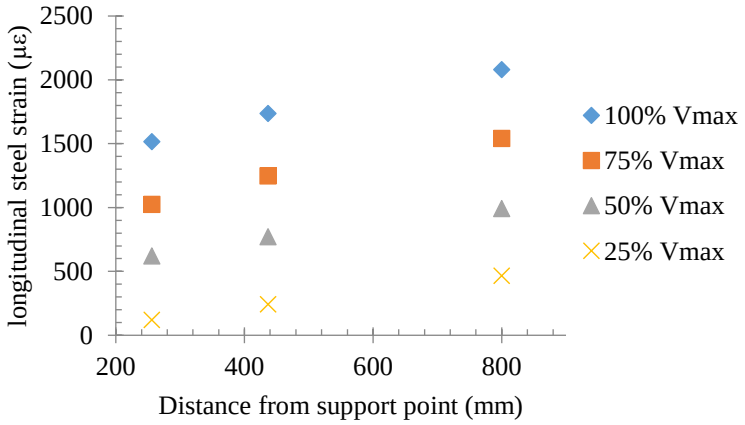

C.

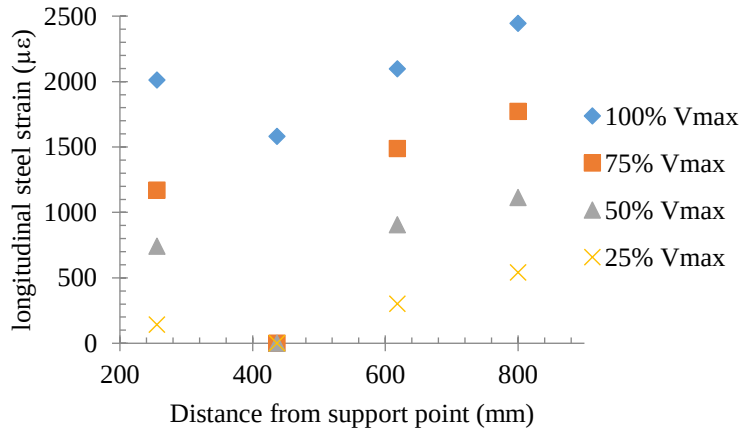

Figure 4.17: Steel strain profile of specimens of group B: A. Specimen ST-C1-90, B. Specimen ST-C2-90, C. Specimen ST-C2-0/90

A.

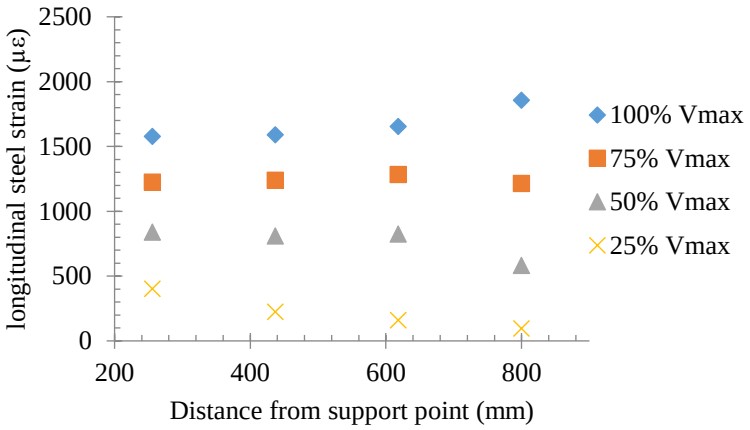

B.

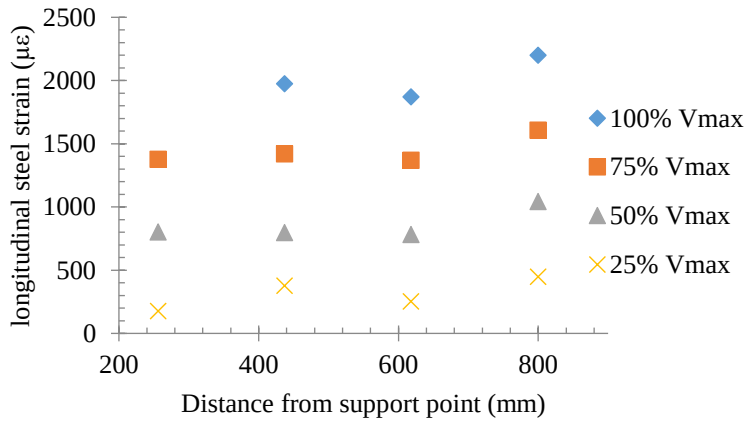

Figure 4.18: Steel strain profile of specimens of group C: A. Specimen NS-G1-90, B. Specimen ST-G1-90

Table 4.6: Maximum measured strain in steel reinforcement

Specimen	$\varepsilon_{s,max}$* (με)	$\varepsilon_{s,max}$ / ε_y**
Control-NS	1014	38%
Control-ST	2614	97%
NS-C1-90	-	-
NS-C2-90	1875	70%
NS-C2-0/90	1719	64%
ST-C1-90	2276	84%
ST-C2-90	2080	77%
ST-C2-0/90	2445	91%
NS-G1-90	1856	69%
ST-G1-90	2200	82%

* At shear capacity ** Yield strain = 2695 με

4.5.2 Stirrup Steel Strains

The strains in the horizontal and vertical steel stirrups were measured at two points in each shear span. In each shear span, one horizontal stirrup and one vertical stirrup were instrumented with strain gauges at the midpoint of the shear span. Figures 4.19 to 4.22 shows the stirrup steel strain responses for all the tested specimens having internal shear reinforcement. Some readings were missing due to damage of the strain gauge before testing. The stirrup strain response comprised two or three phases depending on whether the stirrups have yielded or not prior to failure. In the pre-cracking phase, the stirrups exhibited no or minimal strains. Following cracking, the stirrup strains increased almost linearly until yielding or failure of the beam took place. The third phase occurred only in beams with yielded stirrups. In such a case, the stirrup strain almost plateaued or increased at a higher rate till the beam reached its shear capacity.

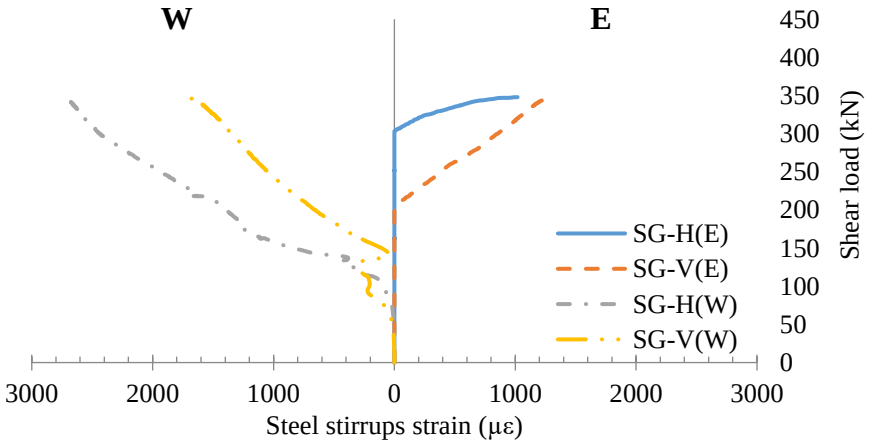

Figure 4.19: Stirrup strain response of specimen Control-ST

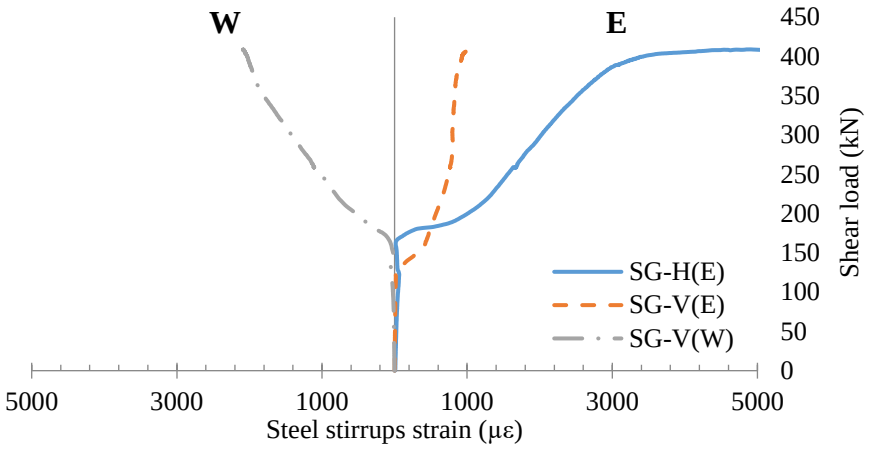

Figure 4.20: Stirrup strain response of specimen ST-C1-90

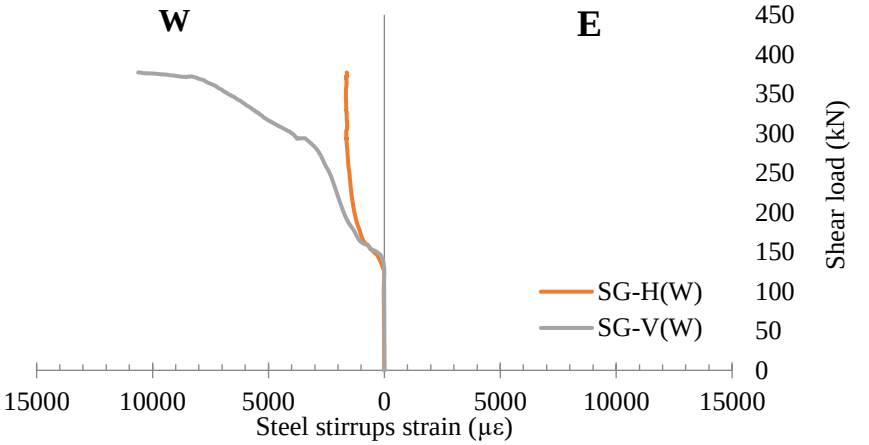

Figure 4.21: Stirrup strain response of specimen ST-C2-0/90

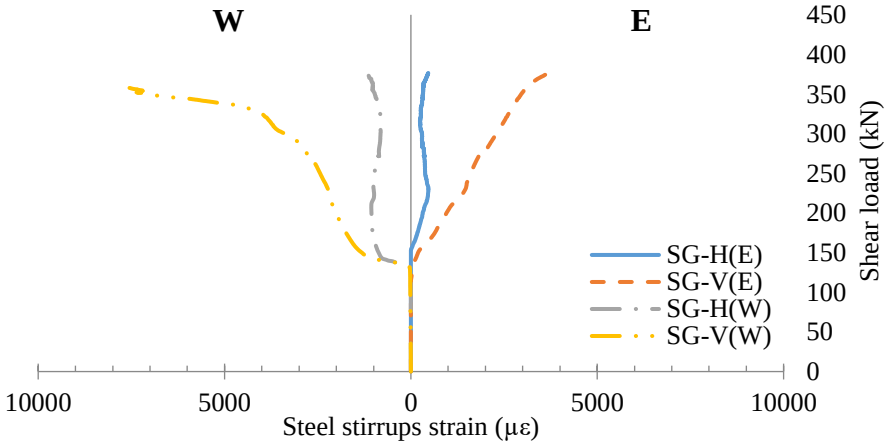

Figure 4.22: Stirrup strain response of specimen ST-G1-90

4.5.3 Carbon Fabric Strains

Strain gauges were installed on vertical carbon fabric bundles located at the center of each shear. The fabric strain responses for all of the strengthened beams are shown in Figures 4.23 to 4.25. Some readings were not obtained because of malfunction of the strain gauges before the test. The fabric strain response of the specimens without internal stirrups consisted of two phases. No or minimal fabric strains were recorded in the pre-cracking phase. After initiation of shear cracks, the fabric started to contribute to the shear resistance, and hence, the fabric strains started to increase almost linearly until the shear capacity was reached. Ideally, specimens with internal stirrups are expected to exhibit a third phase of fabric strain which starts at the onset of yielding of stirrups and ends at peak load. This idealized behavior was evident in the response of some strain gauges bonded to the fabric in specimens with internal steel stirrups. Fabric strain readings confirmed the contribution of the fabric to the shear resistance in the presence of internal stirrups. The shear strength was, however, limited in the presence of internal stirrups because the beams reached their strut capacity shortly after yielding of internal stirrups.

A.

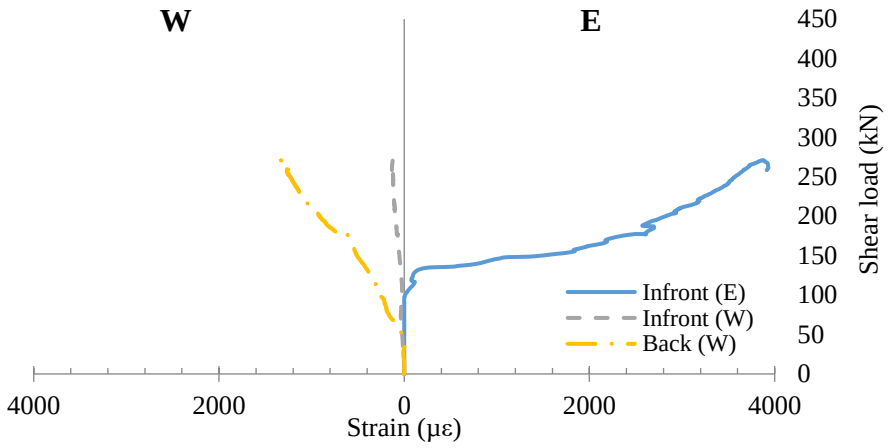

B.

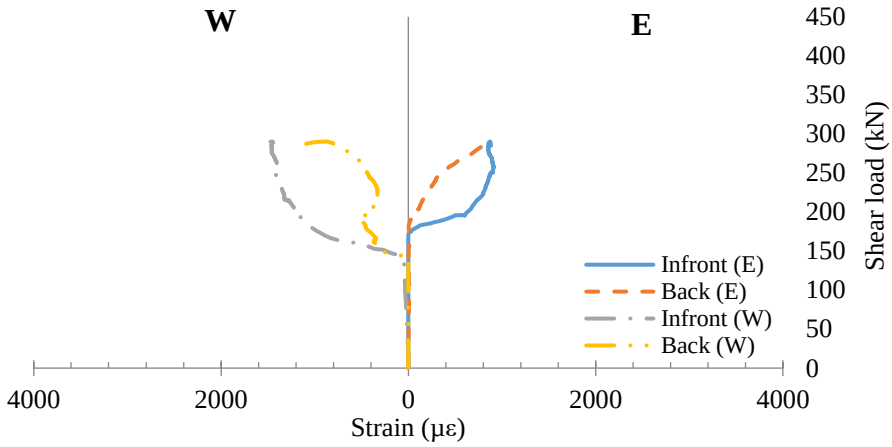

C.

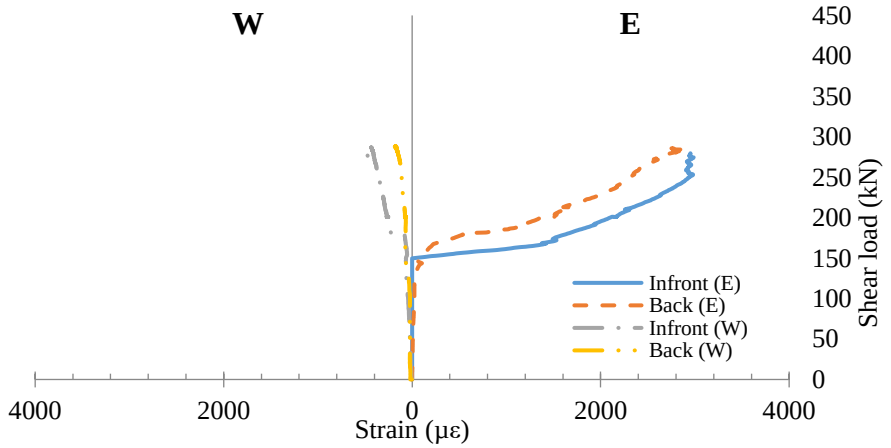

Figure 4.23: Carbon fabric strain response of specimens of group A: A. Specimen NS-C1-90, B. Specimen NS-C2-90, C. Specimen NS-C2-0/90

A.

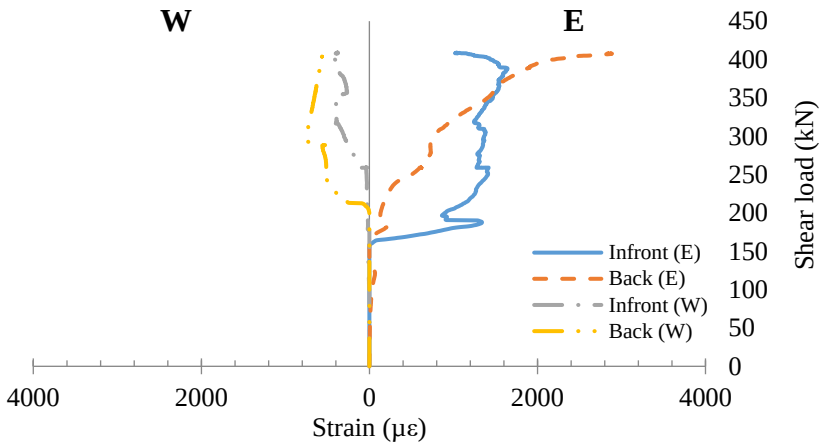

B.

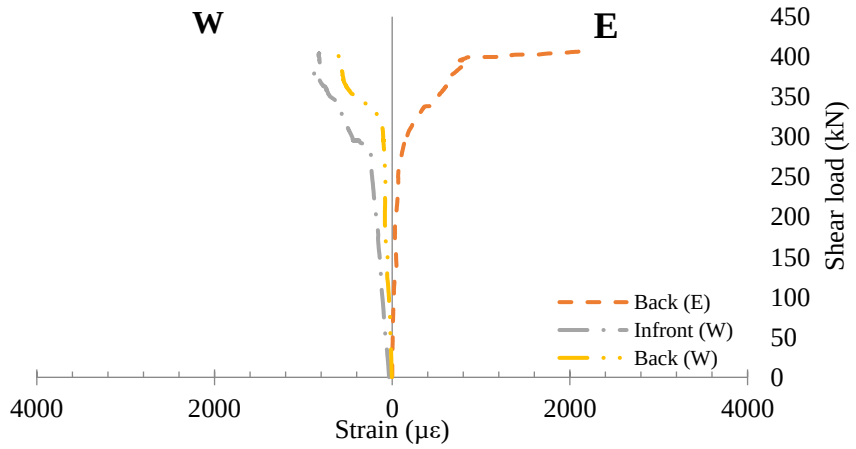

C.

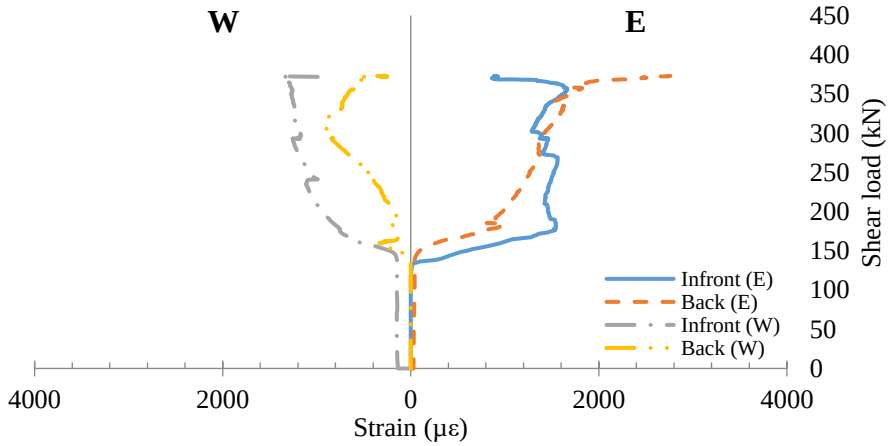

Figure 4.24: Carbon fabric strain response of specimens of group B: A. Specimen ST-C1-90, B. Specimen ST-C2-90, C. Specimen ST-C2-0/90

A.

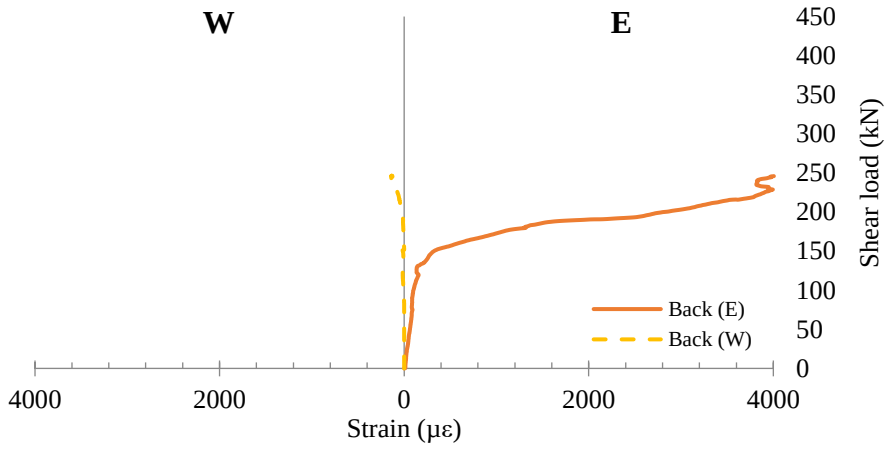

B.

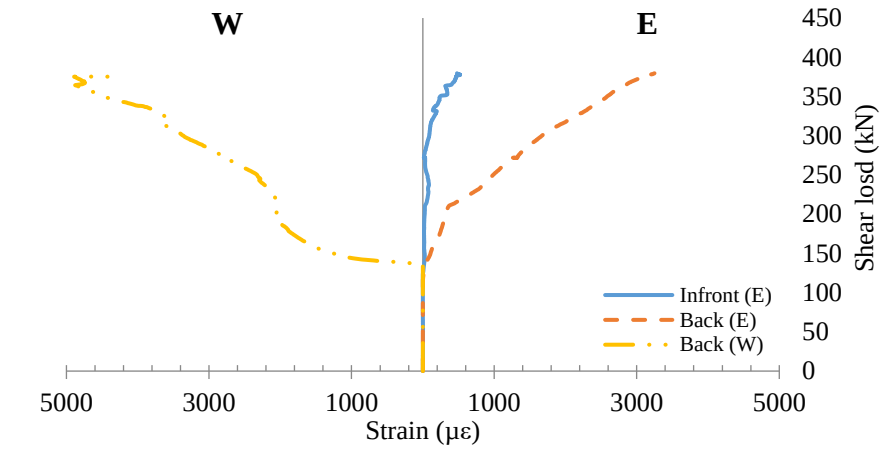

Figure 4.25: Carbon fabric strain response of specimens of group C: A. Specimen NS-G1-90, B. Specimen ST-G1-90

4.5.4 Concrete Strains

Values of maximum measured concrete strains recorded at the shear capacity in the longitudinal and diagonal directions are reported in Table 4.7. All specimens, except NS-C2-90 and NS-C2-0/90, exhibited longitudinal concrete strain values under the load plates higher than those recorded in the diagonal direction at the midpoint of the shear span. The concrete strain in the longitudinal direction at the shear capacity was on average 2127 με with a minimum of 1331 με and a maximum of 3023 με. Specimens NS-C2-90 and NS-C2-0/90 exhibited significant diagonal concrete strains

of 1868 με and 1719 με, respectively, at the shear capacity. The higher concrete strain exhibited by NS-C2-90 and NS-C2-0/90 in the diagonal direction could be ascribed to the increased confinement caused by using two layers of FRCM. Specimen Control-ST, with internal stirrups, exhibited a higher diagonal concrete strain at shear capacity (924 με) than that of its counterpart Control-NS without internal stirrups (562 με). Specimens with internal stirrups strengthened with FRCM composites exhibited diagonal concrete strains values in the range of 619 to 707 με at the shear capacity. The diagonal concrete strain gauge of specimen ST-C2-0/90 failed at 43% of the shear capacity at a value of 463 με. The specimens strengthened with FRGM exhibited higher diagonal concrete strains at the shear capacity than those of their un-strengthened counterparts.

Table 4.7: Maximum concrete strains at shear capacity

Specimen	Longitudinal strain* (με)	Diagonal strain (με)
Control-NS	2341[1]	550
Control-ST	2471	924
NS-C1-90	2172	1320
NS-C2-90	1331	1868[2]
NS-C2-0/90	1395[3]	1719**
ST-C1-90	2193[4]	619[5]
ST-C2-90	1936	707[6]
ST-C2-0/90	1854[7]	463[8]
NS-G1-90	3023	1183[9]
ST-G1-90	2269	1487[10]

* Under the load plates
** Shortly after peak load.
[1] Failed at 94% of shear load
[2] Failed at 91% of shear load
[3] Failed at 96% of shear load
[4] Failed at 98% of shear load
[5] Failed at 95% of shear load
[6] Failed at 97% of shear load
[7] Failed at 86% of shear load
[8] Failed at 43% of shear load
[9] Failed at 98% of shear load
[10] Failed at 86% of shear load

4.6 Summary

Outcomes of the laboratory testing were presented and discussed throughout this chapter. The results included the shear load-deflection response, failure mode, crack pattern, and strain measurements. Details of the numerical models are provided in the next chapter along with a comparative analysis between predicted and experimental results.

Chapter 5 : Numerical Modeling and Simulation

5.1 Introduction

ATENA software [15] was used in this study to predict the nonlinear response of the tested specimens. A bond-slip model at the fabric-matrix interface was included in the analysis. This chapter provides an overview of the material's constitutive laws, element types, and boundary conditions. The effect of inclusion of a bond-slip law at the fabric-matrix interface on numerical results was elucidated. Numerical predictions were compared to experimental results to examine the accuracy of the numerical simulation models.

5.2 Material Constitutive Laws

Concrete and reinforcement mechanical characteristics were utilized as input data to define each material's behavior. The program has built-in material constitutive models. The software allows the user to edit key values of the material constitutive models to input available measured properties of materials.

5.2.1 Concrete Constitutive Models

In this research, the built-in material constitutive models of the concrete "CC3DNonLinCementitious2" was adopted. It allows the user to input the cube compressive strength of the concrete. Then, the program generates the remainder of the concrete characteristics using built-in formulas. Nevertheless, the user can edit and modify essential material constitutive law parameters, including concrete cylinder compressive strength, tensile strength, elastic modulus, etc.

The constitutive laws for tensile (fracturing) and compressive (plastic) behavior are linked in the fracture-plastic concrete model. The fracture model is based on the crack band model, and the orthotropic applied crack formulation. It combines the Rankine failure criterion and exponential softening. On the other hand, the Menétrey-Willam failure surface is used in the hardening/softening plasticity model. For the integration of constitutive equations, the model employs the return mapping algorithm. The algorithm can handle situations where both models' failure surfaces are active, as well as physical changes such as crack closing.

At tension, the stress-strain curve starts with a linear relationship, having a slope equal to the concrete modulus of elasticity (E_c). The relationship remains linear till the tensile stress (σ_t) reaches the concrete tensile strength (f_t). The stress-strain relationship then decreases exponentially, with the crack opening displacement (w_t) calculated from the fracturing strain (ε_f) times the crack band length (L_t) as in Eq (5.1). As illustrated in Figure 5.1, L_t is considered to represent the size of the element projected into the crack direction. The value of crack opening at complete release stress (w_{tc}) is determined by the amount of concrete fracture energy required to generate a unit area of stress-free crack (G_f). The tension stiffening effect in shear-reinforced concrete beams is accounted for through the use of a limiting value of tensile strength in the tension softening branch. In such a case, the tensile strength cannot drop below the product $C_{ts}f_t$, where C_{ts} is a tension stiffness coefficient taken as 0.4.

$$w_t = \varepsilon_f L_t \qquad (5.1)$$

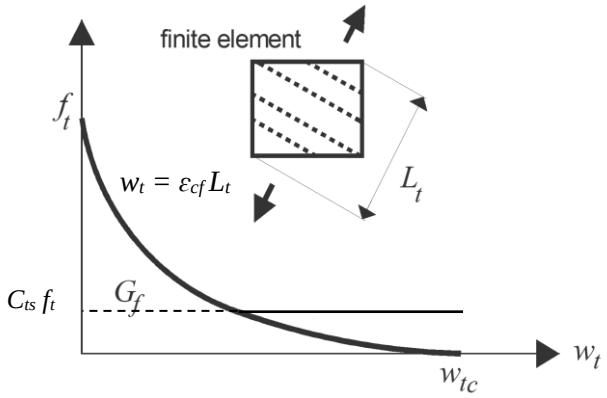

Figure 5.1: Concrete tensile softening

ATENA accounts for the effect of cracks on the shear strength of concrete (τ_{ef}) through the adoption of Eq. (5.2) [15], where a_g denotes the maximum aggregate size, and w denotes the maximum crack width at the specified location.

$$\tau_{ef} = \frac{0.18\sqrt{f'_c}}{0.31 + \frac{24w}{a_g + 16}} \qquad (5.2)$$

Concrete's stress-strain relationship under compression is mainly made up of increasing and decreasing branches. The ascending branch's law is based on strains, whereas the descending branch's law is based on displacements. The rising branch starts with a linear relationship with a slope equal to E_c. Then, it continues up to a compressive stress value of f'_{co} equal to $2\ f'_t$, where E_c is the concrete modulus of elasticity and f'_t is the uniaxial concrete tensile strength. After that, a nonlinear elliptical section continues the curve until the stress exceeds concrete cylinder compressive strength (f'_c). In Equation (5.3), σ_c = compressive stress, f'_{co} = compressive stress at the start of nonlinear compressive behavior, ε_p = plastic strain, and ε_{cp} = plastic strain at compressive strength. The compressive hardening behavior is presented in Figure 5.2.

$$\sigma_c = f_{co} + (f'_c - f_{co})\sqrt{1 - \left(\frac{\varepsilon_{cp} - \varepsilon_p}{\varepsilon_{cp}}\right)^2} \qquad (5.3)$$

$$f'_{co} = 2f'_t \qquad (5.4)$$

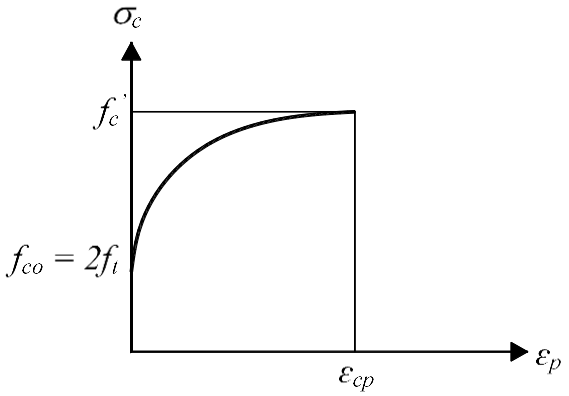

Figure 5.2: Concrete compressive hardening behavior

The concrete compressive stress-strain curve is considered to be linear on the decreasing branch. Therefore, the displacements (w_c) across the length scale (L_c) are inversely proportional to the stress. As given in Eq. 5.5, the displacement w_c is a function of plastic strain (ε_p). As shown in Figure 5.3, ε_{cp} indicates plastic concrete strain at compressive strength, and L_c indicates the projection of element size into the direction of minimal principal stresses. When the displacement equals w_d, the tension is zero, where w_d is the plastic displacement.

$$w_c = (\varepsilon_p - \varepsilon_{cp})\, L_c \qquad (5.5)$$

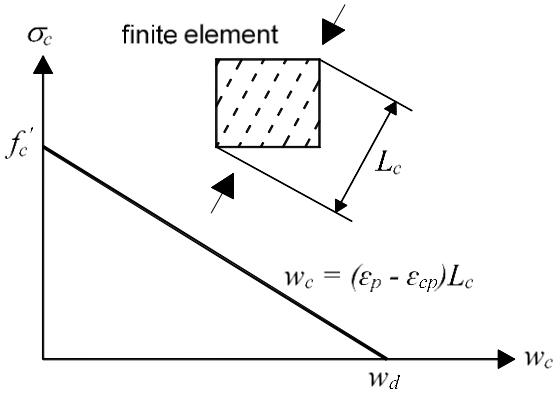

Figure 5.3: Concrete compressive softening

The concrete compressive strength in a direction parallel to the cracks is decreased [15]. The reduced compressive strength ($f'_c{}^{ef}$) is a function of f'_c and the compressive strength reduction factor (r_c), provided by Eq. (5.7) , where ε_1 = strain normal to the crack and r_c^{lim} = minimum value for the reduction factor defined as 0.8.

$$f'_c{}^{ef} = r_c f'_c \qquad (5.6)$$

$$r_c = \frac{1}{0.8 + 170\varepsilon_1}, \quad r_c^{lim} \leq r_c \leq 1 \qquad (5.7)$$

Tables 5.1 to 5.3 show input data used in the numerical analysis for properties of concrete, cementitious and geopolymeric mortars. The cube compressive strength (f_{cu}), measured experimentally, was the primary input. Other key characteristics measured experimentally were included in the input data. The value of the concrete Young's modulus (E_c) was calculated based on the ACI Code [1], whereas respective values for the cementitious and geopolymeric mortars measured experimentally were adopted. Other characteristics were generated by the software using built-in equations based on the value of f_{cu}.

Table 5.1: Concrete properties

Parameter	Description	Value
f_{cu}	Cube compressive strength	-33.5 MPa
f'_c	Cylinder compressive strength	-26.3 MPa
f_t	Tensile strength	2.40 MPa
E_c	Elastic modulus	24.10 GPa
μ	Poisson's ratio	0.2
G_f	Specific fracture energy	$6.229*10^{-5}$ MN/m
c_{ts}	Tension stiffening	0.4
w_d	Critical compressive displacement	$-5*10^{-4}$ m
ε_{cp}	Plastic strain at compressive strength	$-8.968*10^{-4}$

Table 5.2: Properties of cementitious mortar

Parameter	Description	Value
f_{cu}	Cube compressive strength	-42.0 MPa
f'_c	Cylinder compressive strength	-35.3 MPa
f_t	Tensile strength	2.40 MPa
E_c	Elastic modulus	28.9 GPa
μ	Poisson's ratio	0.2
G_f	Specific fracture energy	$7.25*10^{-5}$ MN/m
w_d	Critical compressive displacement	$-5*10^{-4}$ m
ε_{cp}	Plastic strain at compressive strength	$-1.03*10^{-3}$

Table 5.3: Properties of geopolymeric mortar

Parameter	Description	Value
f_{cu}	Cube compressive strength	-43 MPa
f'_c	Cylinder compressive strength	-34 MPa
f_t	Tensile strength	3 MPa
E_G	Elastic modulus	7 GPa
μ	Poisson's ratio	0.2
G_f	Specific fracture energy	$7.364*10^{-5}$ MN/m
w_d	Critical compressive displacement	$-5*10^{-4}$ m
ε_{cp}	Plastic strain at compressive strength	$-1.045*10^{-3}$

5.2.2 Steel Stress-Strain Response

The stress-strain relation of the reinforcing steel bars and steel stirrups was assumed to be with a strain hardening (Figure 5.4). The stress started to increase

linearly proportional to the strain with a slope equals to the young's modulus of steel (E_s) until yielding. The modulus in the strain-hardening stage (E_{sh}) was assumed 1% of E_s. The measured yield strength of the longitudinal steel bars was 539 MPa whereas for the internal stirrups, it was 505 MPa. The value of E_s was 200 GPa.

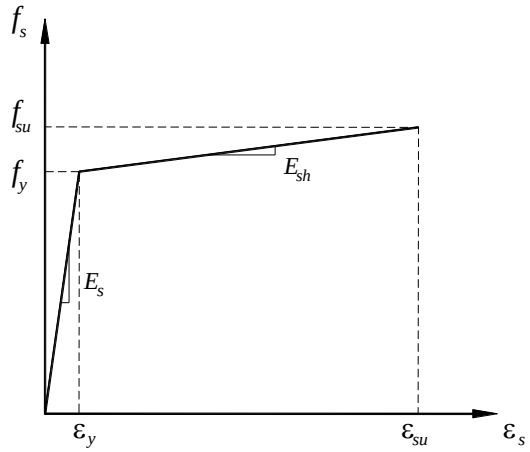

Figure 5.4: Stress-strain of the steel with strain hardening

5.2.3 Carbon fabric Stress-Strain Response

The stress-strain relationship of the carbon fiber bundles was assumed to be linear elastic (Figure 5.5). The carbon fabric used in the current study consisted of unidirectional carbon fiber bundles arranged at spacing of 17 mm. The measured width and thickness of one carbon fiber bundle were approximately 5.0 and 0.54 mm, respectively, which corresponded to a cross-sectional area of 2.7 mm^2. The carbon fiber bundles had a tensile strength of 4,300 MPa and a Young's modulus of 240 GPa (as per the manufacturer data sheet).

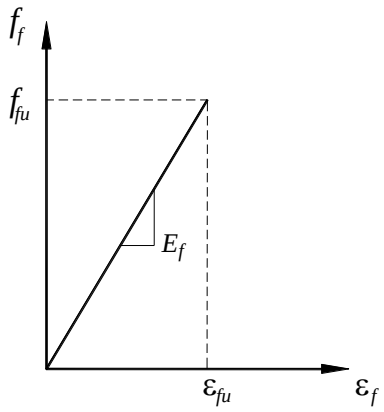

Figure 5.5: Stress-strain response of carbon fabric

5.2.4 Bod-Slip Model

The bond behavior at the fabric-matrix interface is an essential parameter that would affect the effectiveness of FRCM/FRGM composite strengthening system. Two models were created for each specimen strengthened with FRCM/FRGM to investigate the effect of incorporating a bond-slip model between the fabric and the mortar on numerical predictions. In one model, a perfect bond was assumed between the fabric and the mortar, whereas a bond stress-slip model at the fabric-matrix interface was assumed in the other model. The bond stress-slip models developed by Abu Obaida et al. [3] for the same types of fabrics and mortars, shown in Figure 5.6, were adopted in the current study. Perfect bond connection was assumed between the steel reinforcing bars and between the concrete and the mortar.

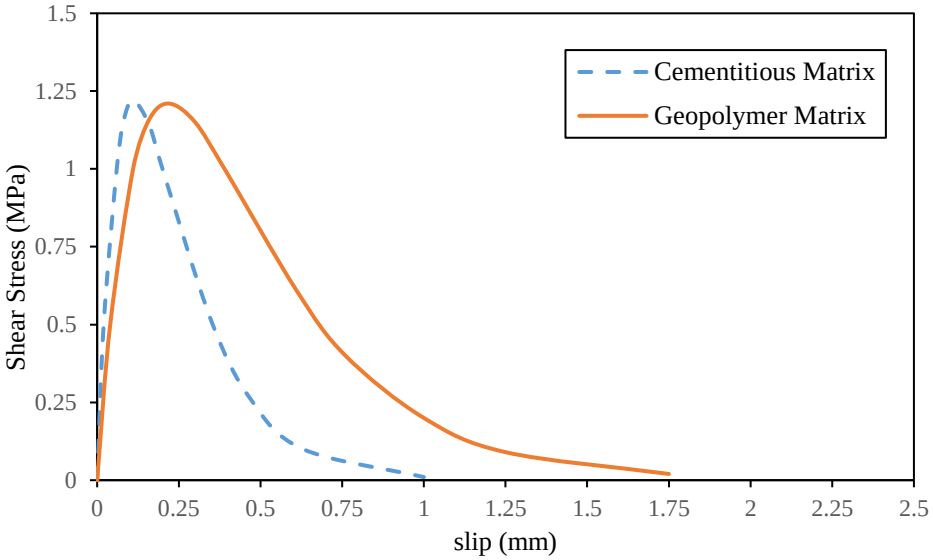

Figure 5.6: Bond-slip models at the fabric-matrix interface [3]

5.3 Element Types

Solid 3D macroelements were used to model the concrete and steel plates. The carbon fiber bundles, longitudinal steel bars, and steel stirrups were individual reinforcement embedded in the concrete macroelements. Such reinforcement is only active in one direction, which is the reinforcement's longitudinal direction. A quarter of the beam was modeled because the beam was symmetric around the middle region throughout the length and width. The mesh size was 20 mm. Further reduction in the mesh size did not result in a significant change in numerical results. Therefore, the model's processing time was raced up by modeling a quarter of the beam with a mesh size of 20 mm. Figures 5.7 to 5.9 show details of the FE models.

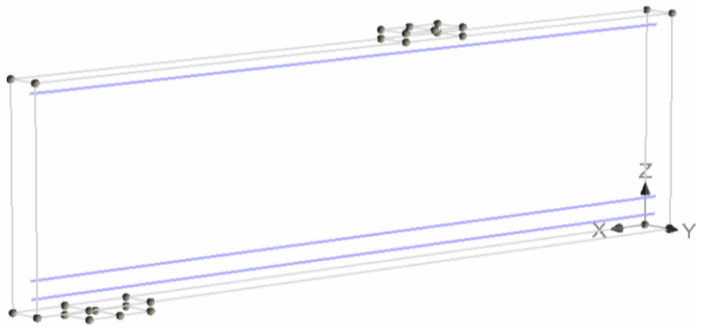

Figure 5.7: Finite element model layout of beams without stirrups

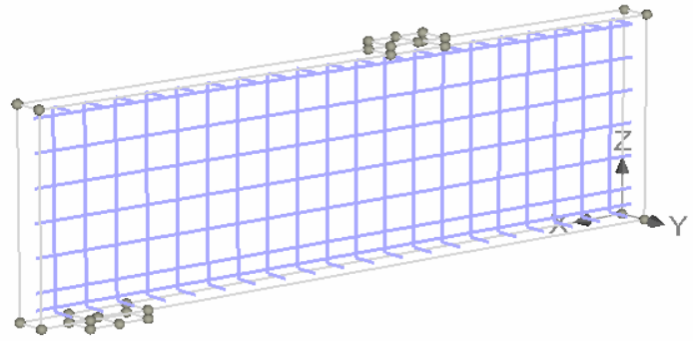

Figure 5.8: Finite element model layout of beams with stirrups

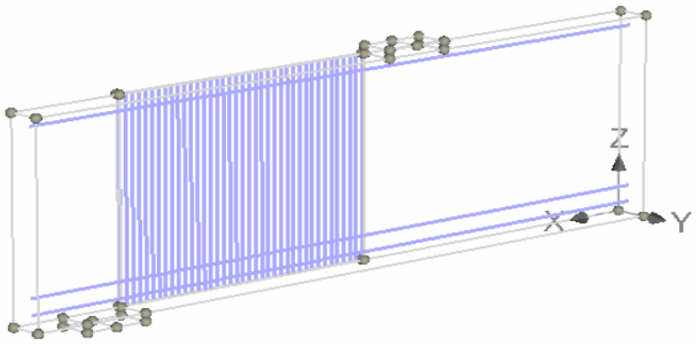

Figure 5.9: Finite element model layout of strengthened beams

5.4 Monitoring Points

Many monitoring points were added to the FE models to obtain the numerical data. The monitoring points were used to measure numerical values for the applied load, midspan deflection, and strains in the steel and carbon fabric reinforcements. Table 5.5 includes the input parameters for all types of monitoring points utilized in

the FE models. The type and value define the intended measurement that will be monitored closest to the monitor location inputs' locations. Also, the component number indicates the direction of the monitored value. For example, X, Y, and Z directions are represented by components 1, 2, and 3, respectively. Figure 5.10 shows examples of monitoring point locations in the FE model.

Table 5.4: Input parameters of monitoring points

Title	Type	Value	Item
Load	Value at node	Reaction	Component 3
Deflection	Value at node	Displacement	Component 3
Steel strain	Value at integration point	Strain	Component 1
Steel stirrups strain	Value at integration point	Strain	Component 1
CFRP strain	Value at integration point	Strain	Component 1

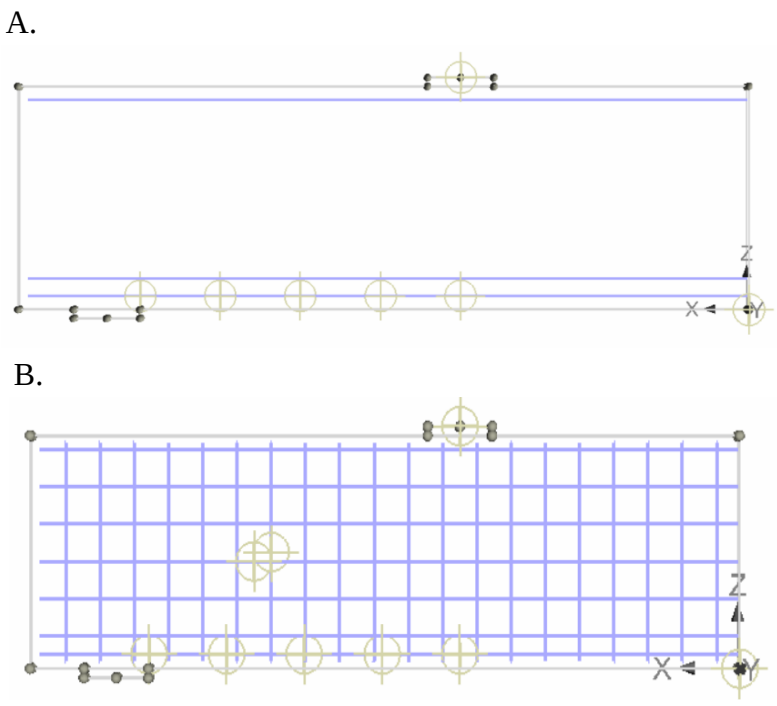

Figure 5.10: Locations of monitoring points: A. Models without stirrups, B. Models with stirrups

5.5 Boundary Conditions and Loading

The established boundary conditions of the quarter model were used to simulate the actual experiment and ensure that the structure was stable. As such, the support plate was restricted from movement in Y (transverse) and Z (vertical) directions. As a quarter of the beam was paraded, surface supports were used to prevent surfaces at planes of symmetry from movement in the direction of the other symmetrical part of the beam, as illustrated in Figure 5.11. The applied load was displacement-controlled loading, described as a vertical displacement at the midpoint of the loading plate's top surface. Each step had a displacement change of 0.1 mm. In the FE analysis, the standard Newton-Raphson iterative solution approach was used.

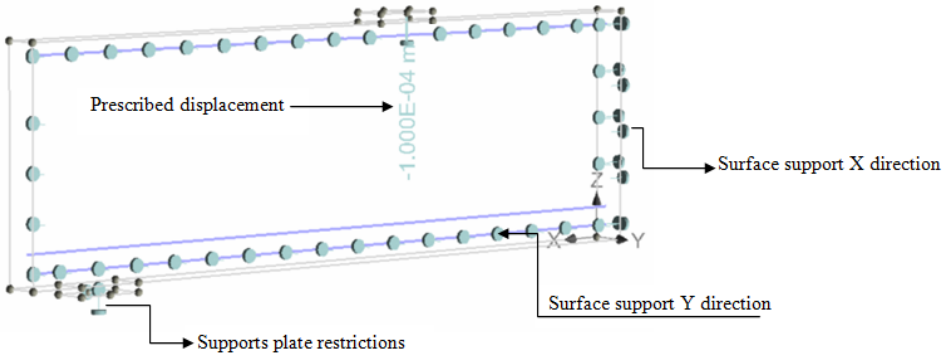

Figure 5.11: Supports and prescribed displacement

5.6 Comparative Analysis

This section presents a comparison between the numerical and experimental results. The shear capacities predicted numerically for the models with and without the bond-slip law are compared to those obtained from the tests in Table 5.6. For the control un-strengthened specimens, the ratio between predicted-to-measured shear capacity was 0.84. For the strengthened specimens, numerical results were within a

20% error band. The ratio of the predicted-to-measured shear capacity had an average value of 0.92 with a corresponding standard deviation of 0.11 and a coefficient of variation of 0.12 for the models without bond-slip, whereas an average value of 0.90 was recorded for the models with bond-slip with a corresponding standard deviation of 0.09 and a coefficient of variation of 0.10.

Numerical results of the strengthened specimens indicated that the inclusion of the bond-slip law at the fabric-matrix interface slightly decreased the predicted shear resistance. In the absence of internal stirrups, the shear capacity of the models with the bond-slip law was on average 7% lower than that of the models with a perfect bond connection at the fabric-matrix interface. The effect of inclusion of the bond-slip law in the analysis was less pronounced in the presence of internal stirrups. In such cases, the inclusion of the bond-slip law resulted in only 2% average shear strength reduction relative to the capacity of the models with perfect bond at the fabric-matrix interface. As such, it can be concluded that the inclusion of the bond-slip law at the fabric-matrix interface yielded more conservative results compared with those of the models with a perfect bond-connection between the fabric and the matrix.

Numerical results of specimens of group A indicated that the use of one layer of FRCM increased the shear capacity of the models without internal stirrups by approximately 2.2 folds. This finding is in agreement with that obtained from the experiments. The numerical results showed that doubling the number of FRCM layers resulted in only 5% to 8% increase in the shear capacity. This finding is in-line with the corresponding experimental results which showed an increase of 7% due to doubling the number of FRCM layers. Similarly, the shear capacity of the counterpart specimens NS-C2-90 and NS-C2-0/90 predicted numerically was significantly

different. Experimental test results verified the insignificant effect of the angle of orientation of the second layer of FRCM on the shear capacity.

Numerical results of specimens of group B indicated that shear strengthening of RC deep beams having internal stirrups with one layer of FRCM resulted in approximately 20% to 22% gain in the shear capacity. The strength gain obtained from the tests was 18%. The strength gain predicted by the model with the bond-slip law at the fabric-matrix interface (20%) was closer to that obtained from the test (18%). The negligible effect of increasing the number of FRCM layers on the shear capacity of specimens of this group was predicted numerically and verified experimentally. The predicted shear capacity of specimen NS-C2-90 was 3% to 5% lower than that of its counterpart specimen NS-C2-0/90. Experimental results of this group verified the insignificant reduction in the shear capacity caused by changing the angle of orientation of the second layer of FRCM from zero to 90^{o}.

Numerical results of specimens of group C (NS-G1-90 and ST-G1-90) and the counterpart specimens from other groups (NS-C1-90 and ST-C1-90) indicated that the use of geopolymers as a matrix instead of the cementitious commercial mortars reduced the shear capacity by 5%. This finding is verified experimentally. corresponding experimental test results showed 7% to 9% reductions in the shear capacity due to the use of the geopolymeric matrix in the strengthening system rather than the cementitious matrix. The agreement between outcomes of the numerical models and those obtained from the experiments verifies the accuracy and validity of the developed FE models.

Table 5.5: Comparison between numerical and experimental results

Group	Specimen	Numerical Result		Experimental Result	V_{FE} (kN) / V_{Exp} (kN)	
		Perfect bond	With bond-slip model		Perfect bond	With bond-slip model
		V_{FE} (kN)	V_{FE} (kN)	V_{Exp} (kN)		
Control	Control-NS	124	N.A.	139	0.89	N.A.
	Control-ST	270	N.A.	348	0.78	N.A.
A	NS-C1-90	283	261	271	1.04	0.96
	NS-C2-90	297	283	290	1.02	0.98
	NS-C2-0/90	295	273	288	1.02	0.95
B	ST-C1-90	329	325	409	0.80	0.79
	ST-C2-90	359	345	411	0.87	0.84
	ST-C2-0/90	341	336	377	0.90	0.89
C	NS-G1-90	269	250	246	1.09	1.02
	ST-G1-90	313	305	380	0.82	0.80
Average					0.92	0.90
Standard deviation					0.11	0.09
Coefficient of variation					0.12	0.10

V_{Exp} = Experimental load capacity
V_{FE} = Predicted load capacity by numerical model

5.6.1 Shear Load-Deflection Response

Figures 5.12 to 5.15 show the numerical prediction of the shear load-deflection responses along with those obtained from the experiments. Numerical prediction of the response of the un-strengthened specimens indicated that the presence of internal stirrups had no effect on the rate of increase of the beam deflection but significantly increased the shear capacity. This outcome is in agreement with that obtained from the tests. The deflections of the specimens at peak load obtained from the numerical models were lower than those measured experimentally because the FE models reached the shear capacity at load values 11% to 22% lower than those recorded experimentally.

Numerical results of specimens of group A indicated that the number FRCM layers and angle of orientation of the second FRCM layer had no effect on the rate of increase of the midspan deflection of the strengthened specimens. This finding is in alignment with experimental observations. The models with the bond-slip law tended to fail at slightly lower values of midspan deflections relative to those of the models with perfect bond at the fabric-matrix interface. The deflections at peak load predicted numerically were on average 20% lower than those obtained from the tests.

The deflection responses of specimens of group B predicted numerically and those obtained from the experiments followed almost same trend. Shear strengthening with FRCM insignificantly increase the stiffness of the specimen. The numerical models failed at lower load, and hence, lower deflections than those obtained from the tests.

Numerical results of specimen of group C confirmed the validity of using geopolymers as a matrix in the strengthening system, which has been verified experimentally. The predicted deflection of specimen NS-G1-90 with the bond-slip law at peak load was 12% lower than that measured experimentally. The corresponding model with the perfect bond at the fabric-matrix interface exhibited 9% lower deflection at peak load relative to that measured experimentally. Models of specimen ST-G1-90 failed at lower loads than those measured experimentally. The reduced predicted shear capacity was accompanied by a reduced deflection at peak load relative to that measured experimentally.

Generally, the ratio of the predicted-to-measured deflection at peak load for was approximately 0.7 for all models with perfect bond including those of the un-strengthened specimens. The models with the bond-slip law at the fabric-matrix

interface exhibited predicted-to-measured deflection ratio at peak load of 0.72 with a standard deviation of 0.11 and a coefficient of variation of 0.15. It should be noted that the measured deflections at peak load were in the range of 6.8 mm to 13.4 mm. Any minor variation between predicted and measured deflections in the order of few millimeters would result in a significant difference in the ratio of predicted-to-measured deflections. Also, actual concrete specimens would include microcracks developed during handling or because of drying shrinkage. The presence of such microcracks would reduce the stiffness of the actual concrete specimens, and hence, increase their deflections relative to those predicted numerically. As such, it can be stated that the models can provide reasonable conservative predictions for the deflection of the beams tested in the present study.

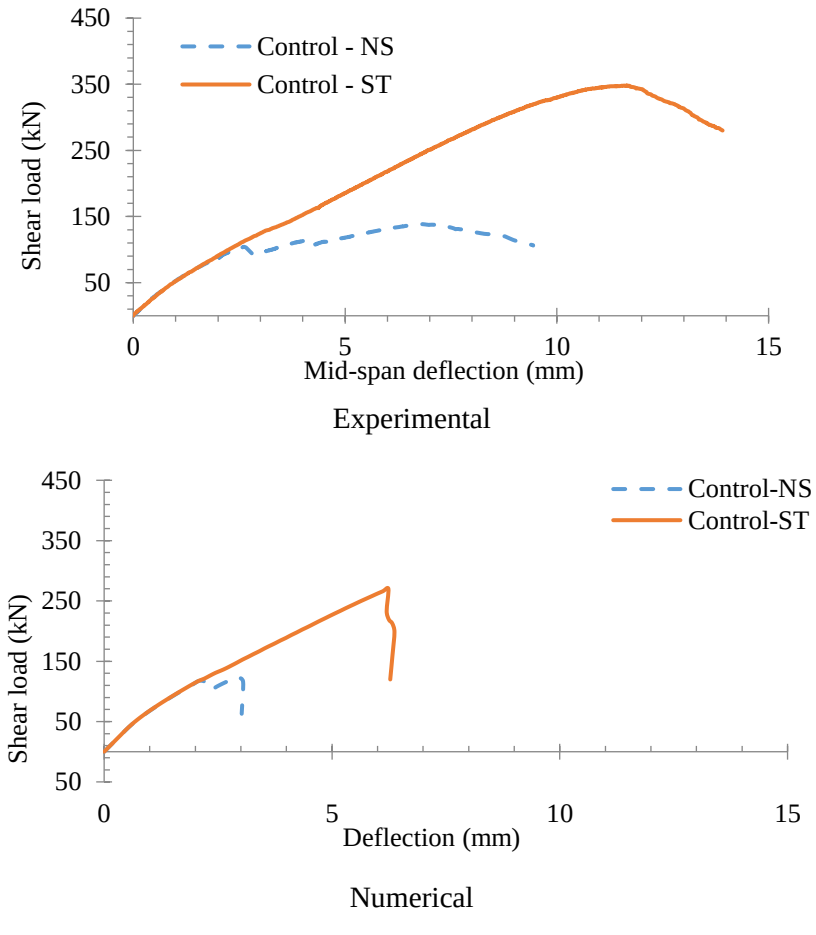

Figure 5.12: Shear load-deflection response of the control specimens

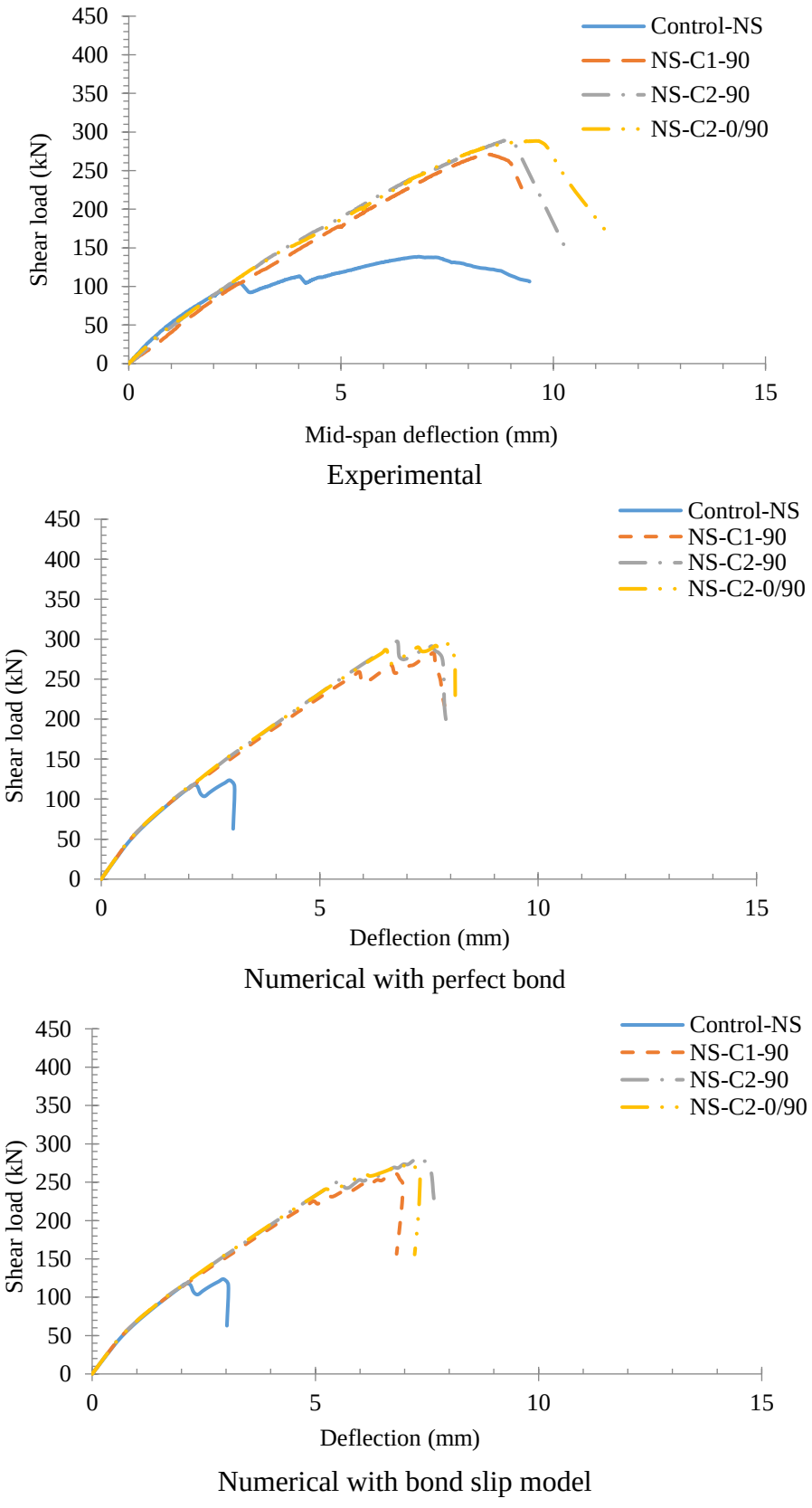

Figure 5.13: Shear load-deflection response for specimens of group A

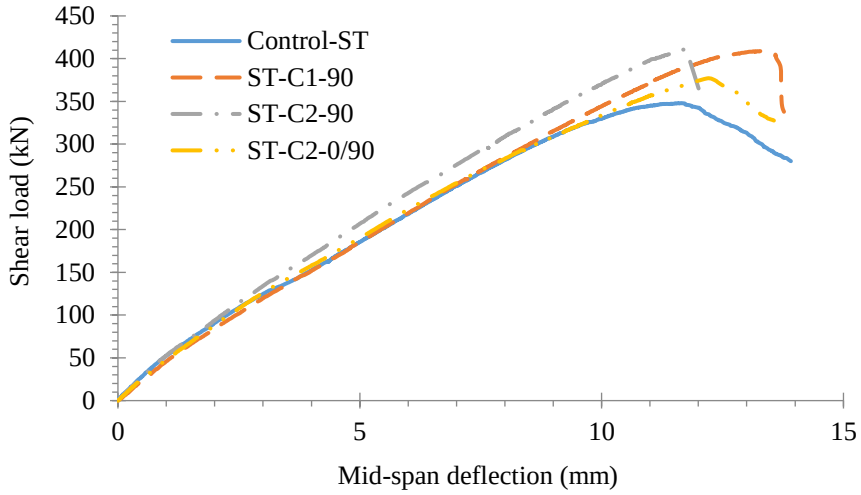

Experimental

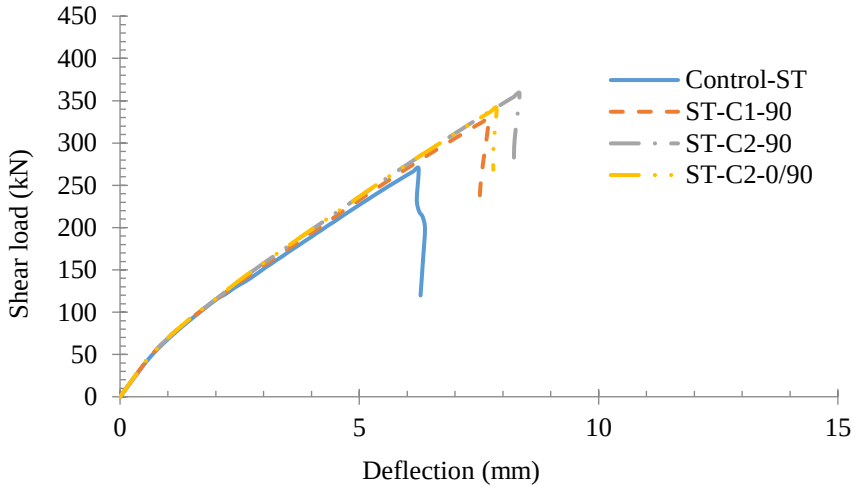

Numerical with perfect bond

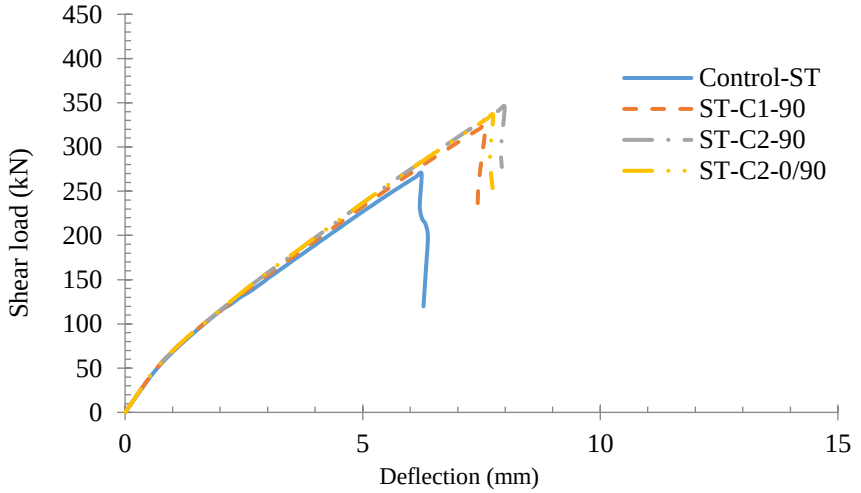

Numerical with bond slip model

Figure 5.14: Shear load-deflection response for specimens of group B

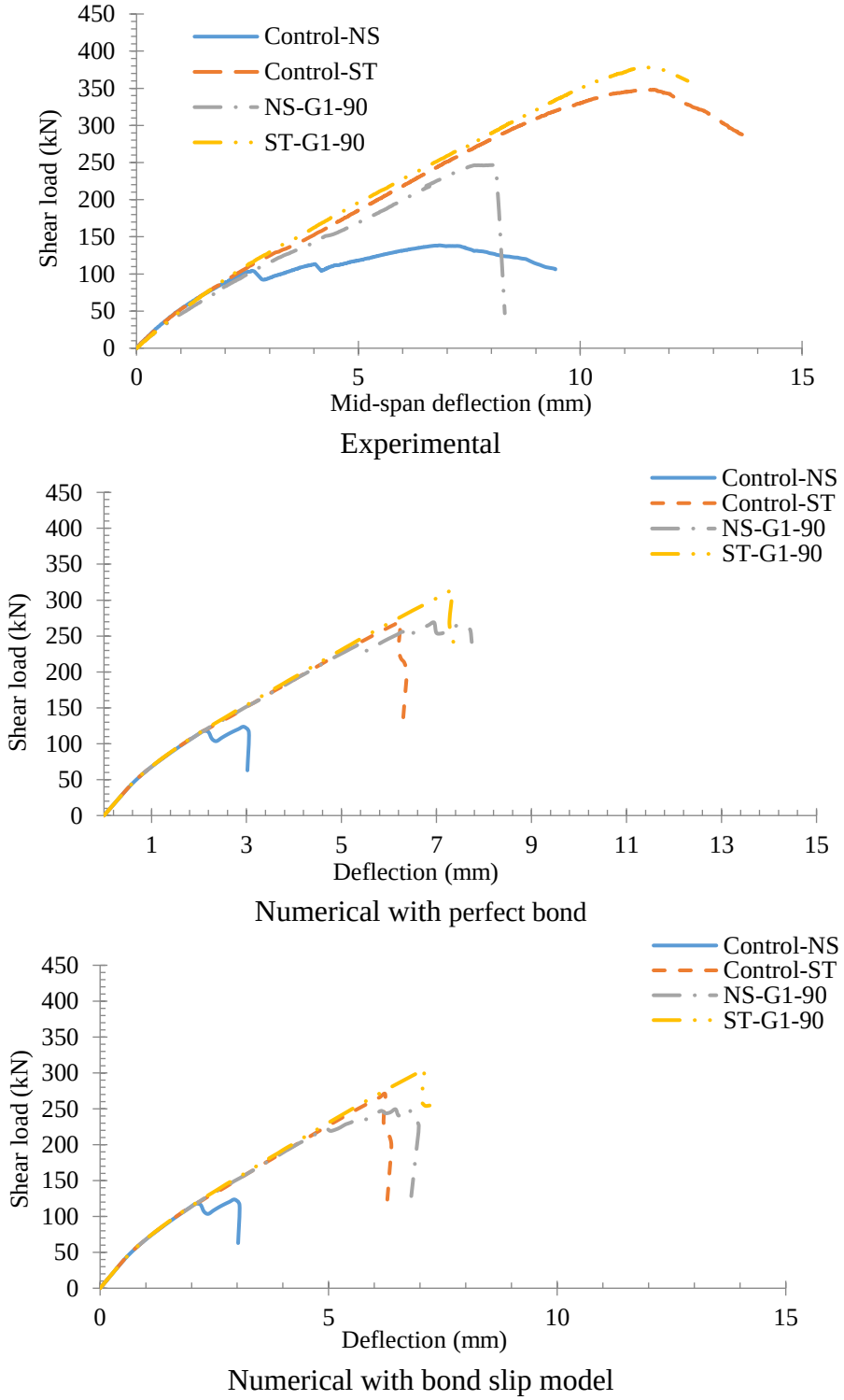

Figure 5.15: Shear load-deflection response for specimens of group C

5.6.2 Crack Pattern

The numerical recorded crack patterns at failure are compared to those of the tests in Figures 5.16 to 5.19. In FE models, cracks with a minimum width 0.1 mm are displayed. The crack patterns predicted numerically are, generally, in good agreement with those observed experimentally.

Numerical Experimental

Control-NS

Numerical Experimental

Control-ST

Figure 5.16: Crack pattern of un-strengthened specimens

Model with perfect bond Model with bond-slip Experimental

NS-C1-90

Model with perfect bond Model with bond-slip Experimental

NS-C2-90

Model with perfect bond Model with bond-slip Experimental

NS-C2-0/90

Figure 5.17: Crack pattern of specimens of group A

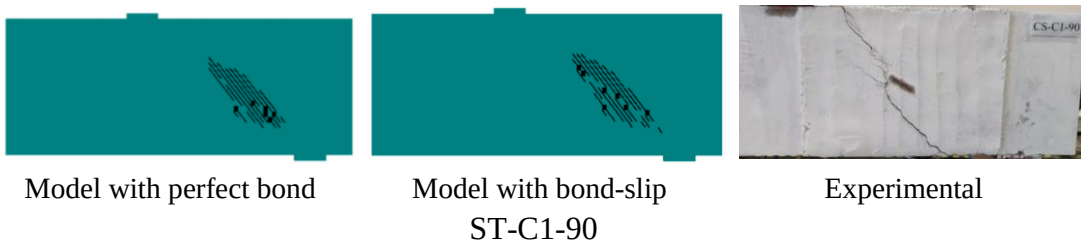

Model with perfect bond | Model with bond-slip | Experimental

ST-C1-90

Model with perfect bond | Model with bond-slip | Experimental

ST-C2-90

Model with perfect bond | Model with bond-slip | Experimental

ST-C2-0/90

Figure 5.18: Crack pattern of specimens of group B

Model with perfect bond | Model with bond-slip | Experimental

NS-G1-90

Model with perfect bond | Model with bond-slip | Experimental

ST-G1-90

Figure 5.19: Crack pattern of specimens of group C

5.6.3 Strains at Peak Load

The strains of the longitudinal steel reinforcement, steel stirrups, and carbon fiber bundles predicted numerically by the models without and with bond-slip law at the fabric-matrix interface are presented in Tables 5.6 and 5.7, respectively. The yield

strain of the steel and the rupture strain of the carbon fiber bundles were 2,695 and 18,000 με, respectively. None of the models exhibited yielding of the longitudinal steel as planned in the design. The strains in the carbon fiber bundles were well-below the rupture strain. This behavior has been verified experimentally since none of the strengthened specimens failed by rupture of the carbon fabric. which is in agreement with experimental observation. It is interesting to notice that the stirrup and carbon fabric strains are affected by the inclusion of the bond-slip law between the fabric and the matrix. Numerical models of strengthened specimens with perfect bond between the fabric and the matrix exhibited higher stirrup strains and lower carbon fabric strains that those of their counterparts with the bond-slip law at the fabric-matrix interface. These results verify the interaction between the internal shear reinforcement and external FRCM shear strengthening. The contribution of the FRCM to the shear resistance was less pronounced in the presence of the bond-slip law between the fabric and the matrix. Such a reduced contribution of the carbon fabrics resulted in an increase in the stirrup steel strains at peak loads. The reduced strain and contribution of the carbon fabric caused by the inclusion of the bond-slip law at the fabric-matrix interface was less pronounced in the presence of internal shear reinforcement.

Table 5.6: Strains at peak load for models with perfect bond

Beams	Steel Reinforcement				Steel Stirrups		Carbon fabric	
	Distance from support point (mm)				V	H	V	H
	256	437	618	800				
Control-NS	418	621	548	532	-	-	-	-
Control-ST	794	1080	1236	1338	1740	986	-	-
NS-C1-90	813	1354	1426	1449	-	-	4509	-
NS-C2-90	882	1182	1369	1497	-	-	2923	-
NS-C2-0/90	744	1320	1427	1505	-	-	4283	2722
ST-C1-90	960	1321	1536	1666	1636	951	1540	-
ST-C2-90	1035	1413	1681	1826	1420	919	1274	-
ST-C2-0/90	963	1316	1546	1730	1577	920	1418	702
NS-G1-90	787	1252	1327	1359	-	-	3748	-
ST-G1-90	899	1250	1461	1574	1593	909	1401	-

Table 5.7: Strains at peak load for models with bond-slip law

Beams	Steel Reinforcement				Steel Stirrups		Carbon fabric	
	Distance from support point (mm)				V	H	V	H
	256	437	618	800				
NS-C1-90	781	1258	1287	1316	-	-	2801	-
NS-C2-90	831	1347	1435	1444	-	-	2103	-
NS-C2-0/90	764	1282	1329	1379	-	-	2587	1863
ST-C1-90	947	1302	1511	1639	1756	1020	1237	-
ST-C2-90	996	1358	1611	1752	1512	986	1082	-
ST-C2-0/90	951	1293	1532	1702	1728	981	1138	675
NS-G1-90	726	1218	1262	1259	-	-	2754	-
ST-G1-90	875	1211	1413	1526	1768	1028	985	-

5.6.3.1 Steel Stirrup Strain Response

The shear load-stirrup strain responses predicted numerically by the models without and with the bond-slip law at the fabric-matrix interface are depicted in Figures 5.20 to 5.21, respectively. The stirrups did not strain in the pre-cracking phase. The stirrup strains in the post-cracking phase were affected by the amount of shear reinforcement. Models with FRCM/FRGM exhibited higher shear cracking load and lower stirrup strains in the post-peak stage, which verified the contribution of the shear strengthening system to the shear resistance. Also, models of specimen ST-C2-90 exhibited lower strains than those of other models because of the increased number of FRCM layers. The inclusion of the bond-slip law at the fabric-matrix interface slightly increased the rate of the stirrup strain in the post-cracking phase.

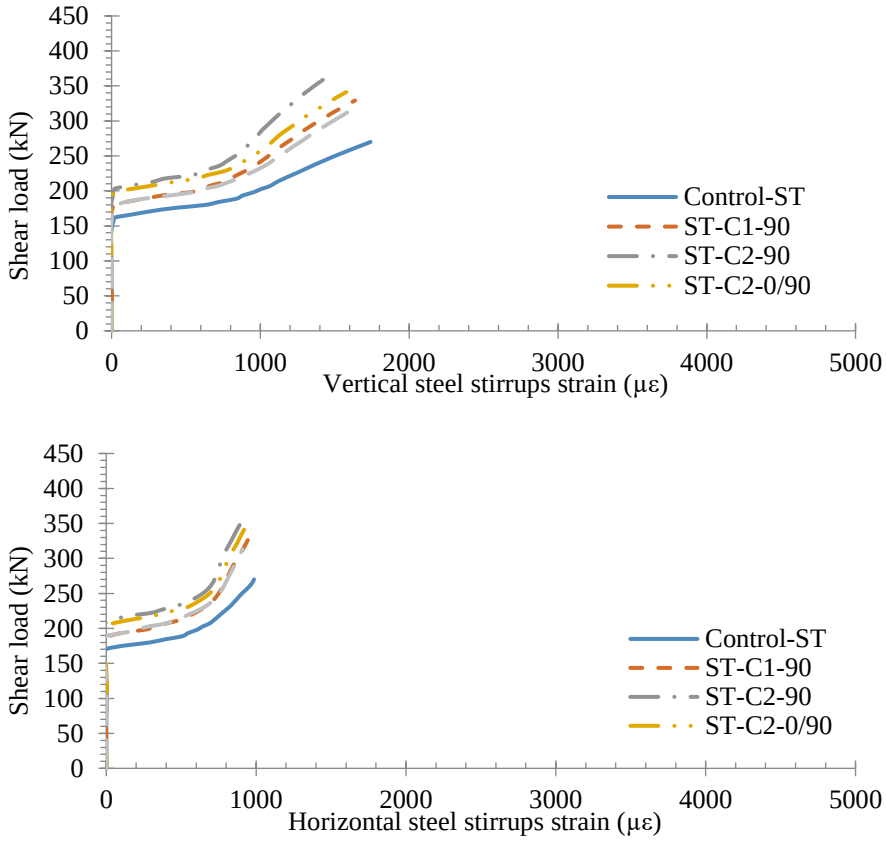

Figure 5.20: Steel stirrup strain response of the models with perfect bond

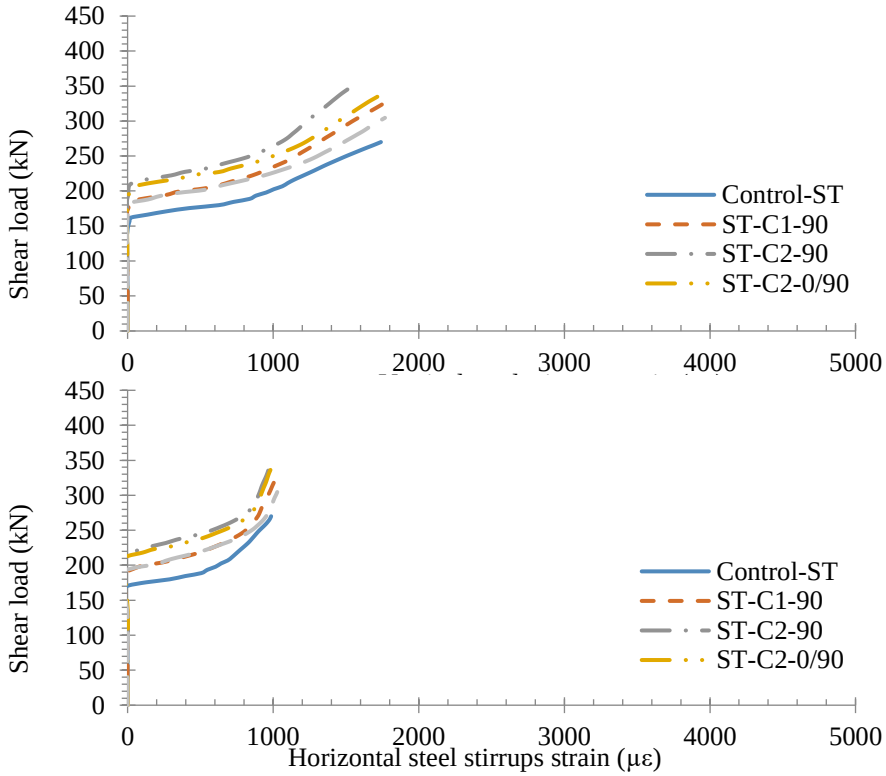

Figure 5.21: Steel stirrup strain response of the models with bond-slip law

5.6.3.2 Carbon Fabric Strain

Figures 5.22 and 5.23 show the fabric strain responses for the models without and with the bond-slip law at the fabric-matrix interface, respectively. Obviously, models without internal stirrups (group A) exhibited higher rates of increase of the carbon fabric strains in the post-cracking stage than those of their counterparts with internal stirrups (group B). The increased rate of carbon fabric strain in the absence of internal stirrups is also evident in models of group C. Models with the bond-slip law at the fabric-matrix interface tended to exhibit lower fabric strains at peak load relative those of their counterparts with perfect bond between the fabric and the matrix.

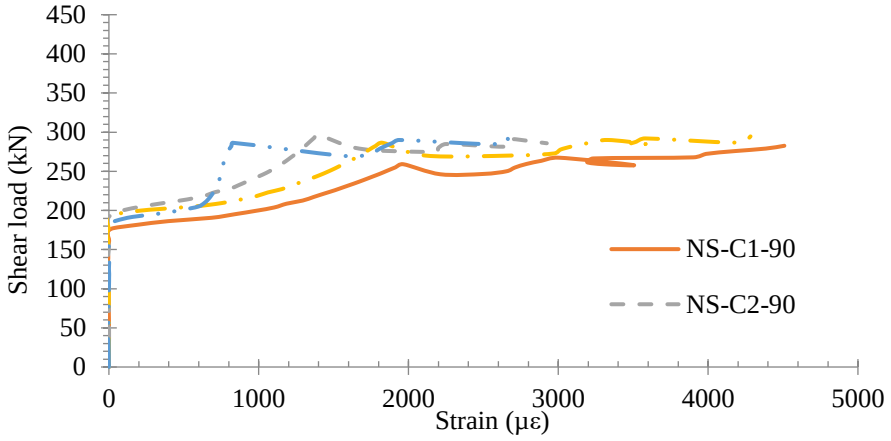

Group A

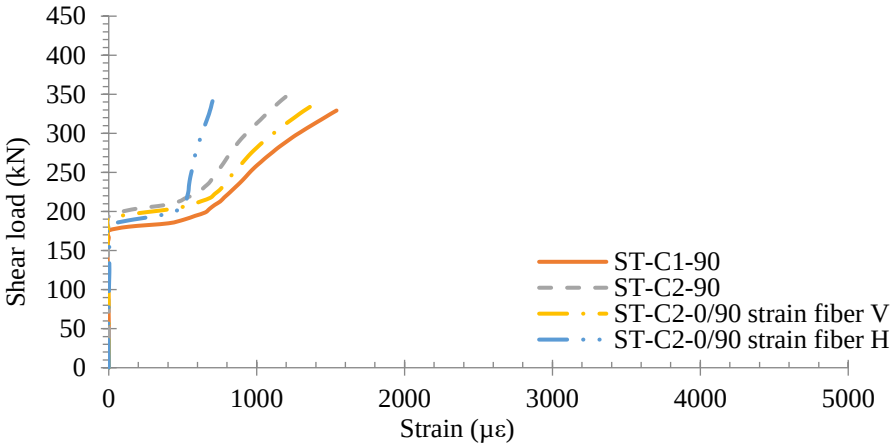

Group B

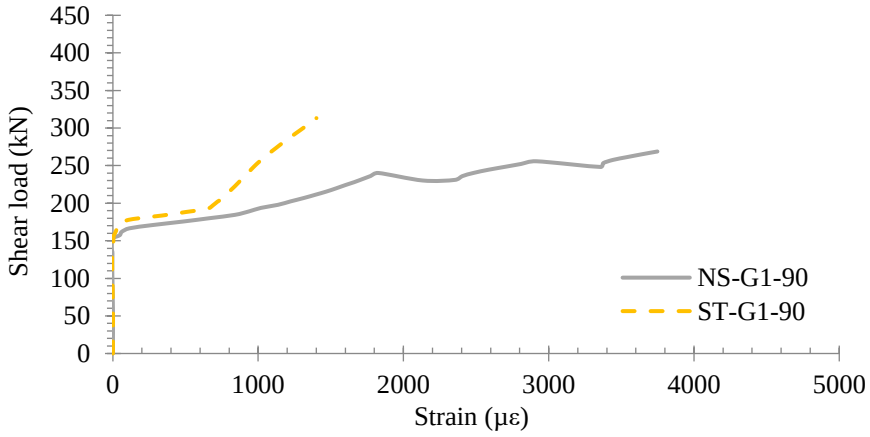

Group C

Figure 5.22: Carbon fabric strain response of the models with perfect bond

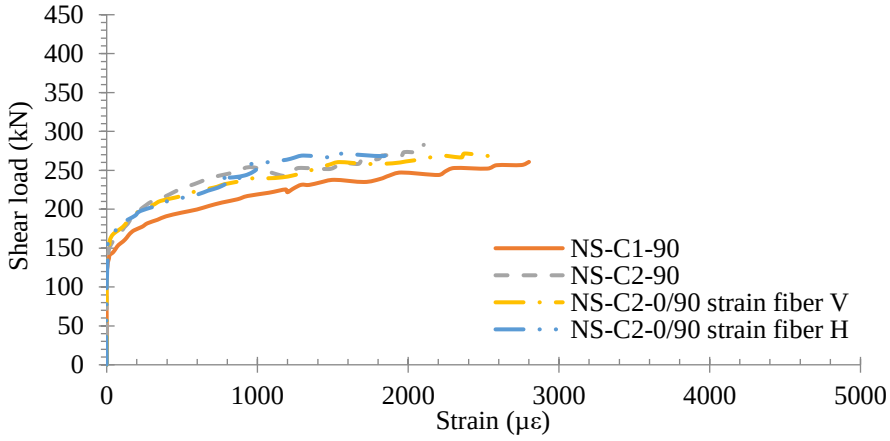

Group A

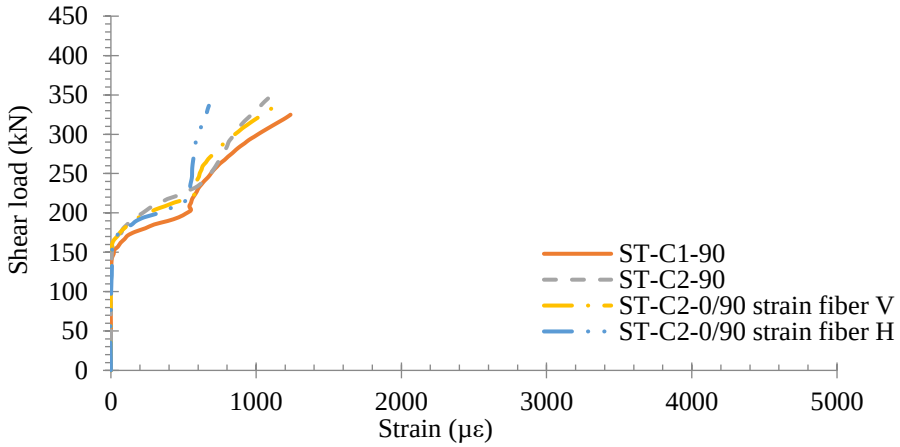

Group B

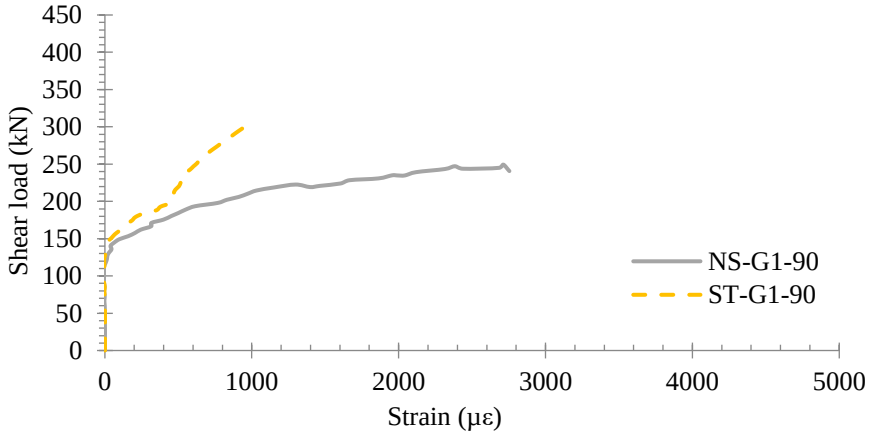

Group C

Figure 5.23: Carbon fabric strain response of the models with bond-slip law

5.7 Summary

The nonlinear structural behavior of the tested specimens was simulated numerically in this chapter using the software ATENA [15]. The accuracy and validity of the numerical simulation models were tested by comparing numerical predictions to experimental data. The limitation of this study, main conclusions of the work, and recommendations for future research are presented in the next chapter.

Chapter 6 : Conclusions and Recommendations

6.1 Introduction

The shear behavior of RC deep beams with *a/h* of 1.6 strengthened with carbon fabric-reinforced matrix was investigated in this research. The study comprised experimental testing and FE modeling. A total of 10 large scale RC deep beam specimens were constructed and tested. Two beams were not strengthened to act as a benchmark. One of the benchmark specimens was reinforced with internal shear reinforcement whereas the other one did not include internal stirrups. Eight beams were strengthened in shear. The shear strengthening system included carbon fabrics along with either a cementitious mortar (C-FRCM system) or a geopolymeric matrix (C-FRGM system). Three-dimensional (3D) FE models were developed for all of the tested specimens. Two FE models were developed for each strengthened specimen. One model included a bond stress-slip law at the fabric-matrix interface whereas a perfect bond connection was assumed between the fabric and the matrix in the other model. The effectiveness of using a geopolymeric matrix as a sustainable alternative rather than the commercial cementitious mortar was examined. The effects of existence of internal shear reinforcement and varying the amount/orientation of the fabric layers on the effectiveness of the shear strengthening system was elucidated. The accuracy and validity of the numerical simulation models developed in the current study to predict the nonlinear shear behavior of RC deep beams strengthened with C-FRCM/C-FRGM were examined. Limitations of the work are highlighted in this chapter along with the main conclusions and recommendations for future studies.

6.2 Limitations of the Current Study

Experimental tests of the current study were conducted on RC deep specimens with specific dimensions and material properties. Therefore, any change in the specimen size and/or properties of the materials used such as steel reinforcement, carbon fabrics, geopolymeric and cementitious mortars may result in different test results. The FE models developed in the present study were, however, capable of predicting the structural response of the tested beams with reasonable accuracy. As such, these FE models may be used as numerical platform to predict the shear response of RC deep beams with different dimensions and material properties.

6.3 Conclusions

The effectiveness of C-FRCM/C-FRGM shear strengthening system to improve the shear behavior of RC deep beams with *a/h* of 1.6 was investigated. The study comprised experimental testing and numerical modeling. Main conclusions of this research work are summarized hereafter:

- The control specimen without internal shear reinforcement failed shortly after initiation of shear cracks in a shear-compression mode of failure. The un-strengthened specimen having internal shear reinforcement failed in a diagonal-compression mode of failure. All strengthened specimens failed due to crushing of the diagonal strut in the shear span (i.e., diagonal compression mode of failure).
- The C-FRCM shear strengthening played a role similar to that of the internal shear reinforcement. In the absence of internal stirrups, one layer of C-FRCM increased the shear capacity by approximately two

folds. Doubling the number of C-FRCM layers insignificantly increased the shear strength gain. Changing the angle of orientation of the second layer of FRCM had an almost no effect on the shear strength gain of the specimens without internal stirrups.

- The shear strength gain caused by the application of C-FRCM was less significant in the presence of internal shear reinforcement. One layer of C-FRCM increased the shear capacity of the specimens with internal stirrups by 18%. Further increase in the number of C-FRCM layers did not result in an additional increase in the shear capacity. Positioning the second layer of carbon fabric in the horizontal direction tended to be less effective than placing it in the vertical direction.
- Test results confirmed the feasibility of using a cement-free geopolymeric matrix rather the commercial cementitious mortar to develop C-FRGM strengthening solution. One layer of C-FRGM resulted in 77% shear strength gain in the absence of internal stirrups and 9% gain in the presence of internal shear reinforcement. The shear capacity of the specimens strengthened with C-FRGM (i.e., with a geopolymeric matrix) was 7% to 9% lower than that of their counterparts strengthened with C-FRCM (i.e., with a cementitious matrix).
- The 3D numerical models developed in the present study were capable of predicting the nonlinear shear behavior of RC deep beams shear-strengthened with C-FRCM/C-FRGM. The inclusion of a bond-slip law at the fabric-matrix interface slightly reduced the contribution of the carbon fabrics to the shear capacity, and hence, results in more

conservative predictions. The reduced contribution of the carbon fabrics to the shear capacity due to the inclusion of the bond-slip law between the fabric and the matrix was less pronounced in the presence of internal stirrups.

- The ratio of the predicted-to-measured shear capacity of the models with perfect bond between the fabric and the matrix was on average 0.92 with a corresponding standard deviation of 0.11 and a coefficient of variation of 12%. The numerical models with a bond-slip law at the fabric-matrix interface yielded more conservative results with an average ratio of predicted-to-measured shear capacity of 0.90, standard deviation of 0.09 and coefficient of variation of 10%.

6.4 Recommendations for Future Studies

This study expanded our understanding of the behavior of RC deep beams strengthened with C-FRCM/C-FRGM systems. The following are suggestions for further research related to this subject:

- Investigate the viability of FRCM/FRGM shear strengthening solution to improve the behavior of RC deep beams with different *a/h* ratios.
- Examine the behavior of RC deep beams with corroded stirrups strengthened with FRCM/FRGM composite-based systems.
- Investigate the effect of varying material properties and section size on the shear behavior of RC deep beams strengthened with composites through a parametric study.

References

[1] ACI Committee 318 and American Concrete Institute (ACI), *Building code requirements for structural concrete (ACI 318-14): an ACI standard and commentary on building code requerements for structural concrete (ACI 318R-14) : an ACI report*. Farmington Hills, Michigan: American Concrete Institute, ACI, 2014.

[2] American Concrete Institute, Ed., *Guide to design and construction of externally bonded fabric-reinforced cementitious matrix (FRCM) systems for repair and strengthening concrete and masonry structures*. Farmington Hills, Mich: American Concrete Institute, 2013.

[3] F. Abu Obaida, T. El-Maaddawy, and H. El-Hassan, "Bond Behavior of Carbon Fabric-Reinforced Matrix Composites: Geopolymeric Matrix versus Cementitious Mortar," *Buildings*, vol. 11, no. 5, p. 207, May 2021, doi: 10.3390/buildings11050207.

[4] L. N. Koutas, Z. Tetta, D. A. Bournas, and T. C. Triantafillou, "Strengthening of Concrete Structures with Textile Reinforced Mortars: State-of-the-Art Review," *J. Compos. Constr.*, vol. 23, no. 1, p. 03118001, Feb. 2019, doi: 10.1061/(ASCE)CC.1943-5614.0000882.

[5] O. Awani, T. El-Maaddawy, and N. Ismail, "Fabric-reinforced cementitious matrix: A promising strengthening technique for concrete structures," *Construction and Building Materials*, vol. 132, pp. 94–111, Feb. 2017, doi: 10.1016/j.conbuildmat.2016.11.125.

[6] O. Awani, T. El-Maaddawy, and A. El Refai, "Numerical Simulation and Experimental Testing of Concrete Beams Strengthened in Shear with Fabric-Reinforced Cementitious Matrix," *J. Compos. Constr.*, vol. 20, no. 6, p. 04016056, Dec. 2016, doi: 10.1061/(ASCE)CC.1943-5614.0000711.

[7] Z. R. Aljazaeri and J. J. Myers, "Strengthening of Reinforced-Concrete Beams in Shear with a Fabric-Reinforced Cementitious Matrix," *J. Compos. Constr.*, vol. 21, no. 5, p. 04017041, Oct. 2017, doi: 10.1061/(ASCE)CC.1943-5614.0000822.

[8] J. H. Gonzalez-Libreros, L. H. Sneed, T. D'Antino, and C. Pellegrino, "Behavior of RC beams strengthened in shear with FRP and FRCM composites," *Engineering Structures*, vol. 150, pp. 830–842, Nov. 2017, doi: 10.1016/j.engstruct.2017.07.084.

[9] R. Azam, K. Soudki, J. S. West, and M. Noël, "Behavior of Shear-Critical RC Beams Strengthened with CFRCM," *J. Compos. Constr.*, vol. 22, no. 1, p. 04017046, Feb. 2018, doi: 10.1061/(ASCE)CC.1943-5614.0000829.

[10] A. Younis, U. Ebead, and K. C. Shrestha, “Different FRCM systems for shear-strengthening of reinforced concrete beams,” *Construction and Building Materials*, vol. 153, pp. 514–526, Oct. 2017, doi: 10.1016/j.conbuildmat.2017.07.132.

[11] T. G. Wakjira and U. Ebead, “FRCM/internal transverse shear reinforcement interaction in shear strengthened RC beams,” *Composite Structures*, vol. 201, pp. 326–339, Oct. 2018, doi: 10.1016/j.compstruct.2018.06.034.

[12] R. Azam, K. Soudki, J. S. West, and M. Noël, “Shear strengthening of RC deep beams with cement-based composites,” *Engineering Structures*, vol. 172, pp. 929–937, Oct. 2018, doi: 10.1016/j.engstruct.2018.06.085.

[13] T. G. Wakjira and U. Ebead, “Internal transverse reinforcement configuration effect of EB/NSE-FRCM shear strengthening of RC deep beams,” *Composites Part B: Engineering*, vol. 166, pp. 758–772, Jun. 2019, doi: 10.1016/j.compositesb.2019.03.004.

[14] “S&P ARMO-mesh® | S&P International.” https://www.sp-reinforcement.eu/en-EU/products/reinforcement-mesh/sp-armo-meshr (accessed Nov. 11, 2021).

[15] V. Červenka, L. Jendele, and J. Červenka, “ATENA Program Documentation Part 1 Theory,” p. 330, Jul. 2017.